

---

# A UNIFIED BACKGROUND-ERROR COVARIANCE MODEL FOR MIDLATITUDE AND TROPICAL ATMOSPHERIC DATA ASSIMILATION

---

Boštjan Melinc<sup>1</sup>, Uroš Perkan<sup>1</sup>, and Žiga Zaplotnik<sup>2,1</sup>

<sup>1</sup>University of Ljubljana, Faculty of Mathematics and Physics,  
Jadranska 19, 1000 Ljubljana, Slovenia

<sup>2</sup>European Centre for Medium-range Weather Forecasts,  
Robert-Schuman-Platz 3, 53175 Bonn, Germany

## ABSTRACT

Estimating background-error covariances remains a core challenge in variational data assimilation (DA). Operational systems typically approximate these covariances through transformations that separate geostrophically balanced components from unbalanced inertio-gravity modes – a framework well-founded in the midlatitudes but less applicable in the tropics, where different physical balances dominate.

We demonstrate that performing DA in the latent space of a neural-network autoencoder yields analysis increments that respect multivariate horizontal and vertical physical balances in both tropical and midlatitude atmosphere. Assimilating a single 500 hPa geopotential height observation in the midlatitudes produces increments consistent with geostrophic and thermal wind balances, while assimilating a total column water vapor observation with a positive departure in the nearly-saturated tropical atmosphere generates an increment resembling the tropical response to (latent) heat-induced perturbations. The resulting increments are localized and flow-dependent, and shaped by the orography and land-sea contrasts. Forecasts initialized from these analyses exhibit realistic weather evolution, including Kelvin wave excitation and its eastward movement in the tropics.

Finally, we explore the transition from using synthetic ensembles and a climatology-based background error covariance ( $\mathbf{B}$ ) matrix to an operational ensemble of background to properly represent flow-dependent “errors of the day”. Despite significant compression-induced variance loss in some variables, latent-space assimilation produces balanced, flow-dependent increments – highlighting its potential for ensemble-based latent-space 4D-Var.

## Keypoints:

- The background-error covariances in a machine learning-based variational data assimilation framework are studied.
- The method captures both tropical and midlatitude atmospheric balances in the background-error covariance model.
- The approach works with both climatological and ensemble-based background-error covariance matrices.

**Keywords** variational data assimilation, background-error covariances, atmospheric balances, tropical data assimilation, neural network data assimilation, latent space

## 1 Introduction

Global weather forecasting is an initial value problem. Given an estimate of the initial state of the atmosphere, the forecast model simulates its evolution [Kalnay, 2002]. The best estimate of the initial state, known as the *analysis*, is obtained through data assimilation (DA). DA combines prior information from a previous short-range forecast (the *background*) with new observations, accounting for their uncertainties and physical constraints. One approach to this problem is Variational Data Assimilation [Lahoz et al., 2010, Park and Xu, 2009], which minimizes the cost function to estimate the analysis. When the background and observations are approximately concurrent, this leads to the three-dimensional variational (3D-Var) formulation.

One of the key challenges in variational DA is the representation of background-error covariances [Bannister, 2008a]. These determine the relative weight of the background and observations and the spread of the information from observations in space and between variables. Analytically, the covariances are encapsulated in a  $\mathbf{B}$ -matrix, which includes the spatial covariances among all model variables. To avoid issues related to  $\mathbf{B}$ -matrix inversion, operational weather centers do not construct and store it but rather define it implicitly using control variable transform (CVT). The balancing terms in CVTs, which map the control variables to model variables, are partly analytical and rely on the assumption that background errors can be adequately characterized by dividing them into vorticity-like components (quasi-balanced, associated with Rossby modes) and divergence-like components (quasi-unbalanced, associated with inertio-gravity modes, Bannister [2008b]).

While geostrophic balance dominates in the extratropical atmosphere, the governing physical balances in the tropics differ significantly due to a weaker Coriolis force. Matsuno [1966] demonstrated that this leads to a rich spectrum of eigenmodes, fundamentally distinct to those in the extratropics. Žagar et al. [2004] therefore proposed to use balance relationships based on equatorial wave theory for tropical DA and demonstrated the effectiveness of this approach in a shallow water model (SWM) on an equatorial  $\beta$ -plane. Building on this, Körnich and Källén [2008] solved the 3D-Var cost function by separating the control variables associated with midlatitude modes and equatorial modes, determined based on the Hough modes (the eigenmodes of the linearised atmospheric motions) of certain equivalent depths and wavenumbers. This framework allowed the system to represent both tropical and extratropical covariances, though with some limitations, such as the incomplete balances. Despite their proven usefulness in diagnostic studies [e.g., Žagar et al., 2005, 2013], the normal modes (the three-dimensional generalization of Hough modes [Kasahara and Puri, 1981]) have not yet been implemented in the operational DA systems. Consequently, the operational weather centers still lack the representation of tropical balances in their systems (e.g., ECMWF [2024]).

Recent years have seen a rapid increase in the use of machine learning (ML) to develop novel DA techniques (see Cheng et al. [2023] and Pasmans et al. [2025] for comprehensive reviews). The idea of using ML for unifying the assimilation procedure in the midlatitudes and the tropics was first proposed by [Melinec and Zaplotnik, 2024, hereafter MZ24], who trained a variational autoencoder (VAE) for reproducing global 850 hPa temperature (T850) fields from ERA5 reanalysis, and performed 3D-Var DA in the reduced-order latent space of a variational autoencoder (VAE). Using single observation experiments, they showed that compressing the T850 into a latent space of 100 elements with a VAE produces a background-error covariance matrix  $\mathbf{B}_z$  that effectively captures local error covariances in both midlatitudes and tropics. Further, despite  $\mathbf{B}_z$  being static and climatological, the background-error covariances in the physical space exhibited state-dependent features. Zheng et al. [2024] then applied the same approach to assimilate sea-surface temperature and demonstrated its feasibility with real-world observations, while Fan et al. [2025] performed 3D-Var and 4D-Var DA in the latent space of a vision transformer. Their analysis increments in the midlatitudes followed the geostrophic balance and were strongly affected by the background flow. Outside of latent-space DA, the physical consistency of analysis increments produced by the ML-based DA techniques received limited attention. Xu et al. [2025] showed that in their system for assimilating satellite observations, an observation with a positive departure of temperature will lead to a physically-consistent decrease in the local relative humidity. Besides, Li et al. [2024] showed physically meaningful analysis increments given the background flow and the time of the observation in their 4D-Var system.

To date, ML-based methods for atmospheric DA were either only deterministic [e.g. Xiao et al., 2023, Chen et al., 2023, Xiang et al., 2024, Sun et al., 2024, Zheng et al., 2024, Fan et al., 2025, Xu et al., 2025], or used statistical or ML methods to directly estimate analysis uncertainty or to generate ensembles of analyses [MZ24, Li et al., 2024, Chen et al., 2024, Andry et al., 2025]. However, none of them leveraged uncertainty information from ensembles of operational forecasts.

In this paper, we present a unified background-error covariance model for data assimilation in both the tropical and midlatitude atmosphere. To achieve this, we extend the approach from MZ24 to a multilevel, multivariate representation of the atmosphere. Section 2 outlines the methodology for 3D-Var data assimilation in the latent space of a neural-network-based autoencoder (AE). Section 3 presents a detailed evaluation of two single observation experiments: one

in the midlatitudes and one in the tropics. We assess their consistency with expected physical balances and run forecasts initialized from the resulting analyses. In Section 4, we estimate the flow-dependent background-error covariance model in the latent by sampling an ensemble of backgrounds from operational ensemble of data assimilations (EDA) from ECMWF’s Integrated Forecasting System (IFS). The discussion and conclusions are provided in Sec. 5.

## 2 Data and methods

Single observation 3D-Var data assimilation experiments and subsequent forecasts were performed using two neural networks with similar architecture and model variables: (1) a convolutional autoencoder (AE) for performing latent-space 3D-Var (Sec. 2.3), and (2) a convolutional U-Net, based on Perkan et al. [2025], used as a neural-network forecasting model to recursively predict the atmospheric states at 12-hour intervals.

### 2.1 Data

The NNs were trained on the ERA5 reanalysis dataset [Hersbach et al., 2020], retrieved from Copernicus Climate Change Service Climate Data Store [2023]. The training set consisted of hourly data from 1970 to 2014, the validation set covered 2015 to 2019, and the test set included 2020 to 2022. Data was downloaded on a regular  $1^\circ \times 1^\circ$  grid and regressed meridionally to avoid the singularities at the poles.

The NNs were trained to reconstruct or predict the variables listed in Table 1. Each physical variable was represented as a  $180 \times 360$  field at each specified level and standardized by subtracting the climatological mean and dividing by the climatological standard deviation, computed individually for each grid point. The dataset included 20 dynamical variables – geopotential height at four levels, zonal and meridional wind at five levels, temperature at four levels, mean sea level pressure, and total column water vapor – and three static variables (land-sea mask, cosine of latitude, and surface elevation) which only served as inputs of the NNs, but were not part of their output.

Table 1: Fields used as inputs to the neural networks. The static fields at the bottom of the table (italicized) are excluded from the output. Surface temperature is a composite of soil temperature over land and sea surface temperature. The abbreviations are written in the same order as the levels.

Quantity [unit]	Levels	Abbreviation
Geopotential height [m]	250 hPa, 500 hPa, 700 hPa, 850 hPa	Z250, Z500, Z700, Z850
Zonal wind [m/s]	200 hPa, 500 hPa, 700 hPa, 900 hPa, 10 m	U200, U500, U700, U900, U10m
Meridional wind [m/s]	200 hPa, 500 hPa, 700 hPa, 900 hPa, 10 m	V200, V500, V700, V900, V10m
Temperature [K]	500 hPa, 850 hPa, 2 m, surface	T500, T850, T2m, ST
Mean sea level pressure [hPa]	-	MSLP
Total column water vapor [ $\text{kg/m}^2$ ]	-	TCWV
<i>Land-sea mask</i>	-	-
<i>Latitude</i>	-	-
<i>Surface elevation</i>	-	-

### 2.2 Neural networks

The autoencoder (AE) consists of an encoder, which compresses the input into a latent representation, and a decoder, which reconstructs the original data from this compressed form. The standardized atmospheric state with shape  $23 \times 180 \times 360$  is first passed through the encoder  $E$  to obtain the *latent vector*  $\mathbf{z}$  containing 12100 elements. The latent vector is then input to the decoder  $D$ , which maps it back to the standardized physical space. The quality of the reconstruction is visualized in Fig. C1.

Similarly to the AE, the input fields are first compressed and then decompressed in a U-Net. Additionally, each encoder block is directly connected to its corresponding decoder block with the same field resolution via skip connections. These connections allow fine-scale spatial information to bypass the compression bottleneck, improving reconstruction

accuracy, especially for localized features [Ronneberger et al., 2015]. An example of the forecast quality is provided in Fig. C2. The technical details of the two applied neural networks are provided in A.

### 2.3 3D-Var in a latent space of an autoencoder

Three-dimensional variational data assimilation (3D-Var) estimates the most likely state of the atmosphere, the *analysis*, by optimally combining information from the previous short-range forecast, the *background*, with new observations. As shown in MZ24, the background state  $\mathbf{x}_b$  can be represented in the AE's latent space as  $\mathbf{z}_b = E \circ S(\mathbf{x}_b)$ , and the analysis  $\mathbf{z}_a$  is obtained by minimizing the cost function

$$\begin{aligned} J_z(\mathbf{z}) &= \frac{1}{2} (\mathbf{z} - \mathbf{z}_b)^\top \mathbf{B}_z^{-1} (\mathbf{z} - \mathbf{z}_b) \\ &\quad + \frac{1}{2} \{ \mathbf{y} - H[S^{-1}(D(\mathbf{z}))] \}^\top \mathbf{R}^{-1} \{ \mathbf{y} - H[S^{-1}(D(\mathbf{z}))] \}, \end{aligned} \quad (1)$$

where  $\mathbf{z}$  is the latent vector and  $\mathbf{B}_z$  is the background-error covariance matrix in the AE's latent space. The vector  $\mathbf{y}$  represents the observations,  $H$  is the observation operator (in our case a bilinear interpolation),  $D$  denotes the decoder and  $E$  the encoder,  $S$  is the standardization operator,  $S^{-1}$  its inverse (destandardization), and  $\mathbf{R}$  is the observation-error covariance matrix.

The derivation of the cost function  $J_z$  assumes that background errors are Gaussian and unbiased. MZ24 avoided the potential issues with these assumptions by applying the cost function (1) in a latent space of a VAE, which ensured the Gaussian properties of the latent vector. In contrast, a “standard” autoencoder does not guarantee Gaussianity in its latent space. However, the latent vectors obtained by encoding the atmospheric states from the validation set exhibited near-Gaussian behavior, with a mean absolute skewness of latent elements of 0.12 and mean absolute kurtosis of 0.19. These values indicate that the latent space is sufficiently close to Gaussian for the latent-space 3D-Var formulation to remain valid.

We also assessed the bias in background  $\mathbf{z}_b$  provided by the 24-hour forecast using the NN forecasting model. For each latent vector element, we compared the mean and standard deviation of the forecast error using forecasts initialized from the atmospheric states in the validation set at 1-hour intervals (Fig. C3a). The background (and so its errors) can be considered unbiased since for most latent vector elements, the error standard deviation vastly exceeded the mean. In a few latent vector elements, the mean approached but did not exceed the standard deviation, indicating some bias, which we assumed negligible for this study.

We preconditioned the minimisation problem by taking  $\chi = \mathbf{L}_z^{-1}(\mathbf{z} - \mathbf{z}_b)$  and square-root preconditioner  $\mathbf{L}_z = \mathbf{B}_z^{1/2}$  and rewrote the cost function (1) into

$$\begin{aligned} J_\chi(\chi) &= \frac{1}{2} \chi^\top \chi \\ &\quad + \frac{1}{2} \{ \mathbf{y} - H[S^{-1}(D(\mathbf{z}_b + \mathbf{L}_z \chi))] \}^\top \mathbf{R}^{-1} \{ \mathbf{y} - H[S^{-1}(D(\mathbf{z}_b + \mathbf{L}_z \chi))] \}, \end{aligned} \quad (2)$$

Minimizing  $\chi$  instead of  $\mathbf{z}$  reduces the condition number, leading to more stable minimisation and fewer iterations to achieve convergence [Bannister, 2008b]. Further technical details on the minimization algorithm are provided in B.

### 2.4 Modelling background-error covariances

The climatological background-error covariance matrix for the experiments in Sec. 3 was computed as

$$\mathbf{B}_z^{clim} = \left\langle (\mathbf{z}_b - \mathbf{z}_t) (\mathbf{z}_b - \mathbf{z}_t)^\top \right\rangle, \quad (3)$$

where  $\mathbf{z}_b$  is the encoded 24-hour NN forecast that served as the background,  $\mathbf{z}_t$  denotes the encoded ground “truth” (i.e., the encoded ERA5 reanalysis for a chosen date and time), and the brackets denote averaging of the outer product over the entire validation set. The details on the computation and properties of the background-error covariance matrix from the operational IFS ensemble of backgrounds within its EDA are provided in Section 4.

In MZ24, the  $\mathbf{B}_z$ -matrix was quasi-diagonal and retaining only its diagonal elements for inversion had no negative impact on the assimilation result. Similar findings were reported by Zheng et al. [2024] and Fan et al. [2025]. In our case, the diagonal elements of  $\mathbf{B}_z$  were typically two orders of magnitude larger than the off-diagonals (Fig. C3b). This allowed us to approximate  $\mathbf{B}_z^{1/2}$  and  $\mathbf{B}_z^{-1/2}$  using only the diagonal, which greatly simplified the computation.

### 3 Single observation experiments

We present two single-observation experiments that illustrate the balance properties of the background-error covariance model in the midlatitudes and the tropics, and demonstrate their physical consistency. Each experiment applies a 24-hour forecast initialized from ERA5 reanalysis data on April 14, 2020 at 00 UTC, which is then encoded into latent space. We generated 100-member ensemble of backgrounds by perturbing this encoded forecast using variances from the  $\mathbf{B}_z$ -matrix. Each perturbed background member has a corresponding perturbed observation set  $\mathbf{y}_\zeta$ . This is obtained by first decoding and destandardizing the background ensemble members, computing their mean and then interpolating it to the observation location. We then added the preset observation departure  $\mathbf{d}$  to that mean and perturbed the output according to the observation standard deviation. The procedure can be described as:

$$\mathbf{y}_\zeta = H(\langle S^{-1} \circ D(\mathbf{z}_b) \rangle) + \mathbf{d} + \boldsymbol{\zeta}_o, \quad (4)$$

where  $\boldsymbol{\zeta}_o \sim \mathcal{N}(\mathbf{0}, \mathbf{R})$  denotes the random vector sampled from a zero-mean and diagonal observation-error covariance matrix.

Each of the 100 pairs of perturbed background and observations was used in a separate 3D-Var DA, resulting in 100 latent-space analyses. The resulting analysis increment  $\delta \mathbf{x}_a$  was computed as the mean of the differences between the decoded analysis and the decoded background, i.e.

$$\delta \mathbf{x}_a = \langle S^{-1} \circ D(\mathbf{z}_a) - S^{-1} \circ D(\mathbf{z}_b) \rangle. \quad (5)$$

The notation in this section and Sec. 4 is organized as follows: the observation departure of a variable  $V$  is labeled as  $d^V$ , the standard deviation of the observation is  $\sigma_o^V$ , the analysis increment is  $\delta_a^V$ , the analysis standard deviation is  $\sigma_a^V$ , and the background standard deviation is  $\sigma_b^V$ . The abbreviations are the same as in Table 1.

#### 3.1 Background-error covariance model in the midlatitudes – geostrophic and thermal wind balance

In the midlatitudes, large-scale atmospheric flow above the planetary boundary layer tends to follow geostrophic balance. Assimilating an observation in this region should, in a well-tuned DA system, yield analysis increments that largely preserve this balance. To evaluate the physical realism of our DA system, we assimilated a single geopotential height observation at 500 hPa (Z500), and studied the resulting analysis increment and the adjustment of the NN forecasting model to the induced perturbation.

We first simulated the Z500 observation above Ljubljana, Slovenia, ( $46.1^\circ\text{N}$ ,  $14.5^\circ\text{E}$ ) with departure of  $d^{Z500} = 30\text{ m}$  and standard deviation of  $\sigma_o^{Z500} = 10\text{ m}$ . Figure 1 shows the analysis increments for selected variables, with the full output provided in Fig. C4. At the 500 hPa pressure level, where the observation was assimilated, the geostrophic balance is evident: a positive Z500 analysis increment centered on the observation location is accompanied by an anticyclonic wind increment (Fig. reffig:Ljubljanaa) and a positive temperature increment from the surface to the observation level (Fig. 1b,c). The T500 increment is nearly isotropic, while the T2m increment's shape is affected by the land-sea distribution, with the larger increments over the land areas, where the background-error standard deviations are larger (Fig. C4, panel C7). An eastward tilt of temperature increments and a westward tilt of geopotential increments with height, in accordance with the quasi-geostrophic theory of developing Rossby waves, further proves the physical plausibility of the analysis increments (Fig. C4, row B).

A positive MSLP increment is located eastward of the maximum geopotential height increment. This is due to (1) negative (anticyclonic) relative vorticity advection and (2) large-scale convergence in the upper-troposphere on the eastern side of the Rossby wave ridge, which leads to an increase in the surface pressure below. A slight distortion of the increment is due to interaction with the orography (Alps, Dinaric Alps).

The geopotential height increment extends vertically (Fig. 2a), with its magnitude increasing with elevation. This is expected, as geopotential height is a vertical integral of temperature, and the positive temperature increments (shown in Fig. 1b,c) accumulate with height. To measure the relative impact of the observation on the analysis, we define it as  $\mathcal{I}^V = \|\delta_a^V\|/\sigma_a^V$ , where  $V$  is the variable of interest. Figure 2d-f shows the crossections of  $\mathcal{I}^{Z500}$ ,  $\mathcal{I}^{U500}$ , and  $\mathcal{I}^{V500}$ , normalized with  $\mathcal{I}^{Z500}$  value at the observation location. Despite Z500 analysis increment rising vertically, the relative impact of the observation peaks at the observation level, and diminishes with distance (Fig. 2d). Similar patterns for increment magnitude and observation impact are observed for both horizontal wind components (Fig. 2b,c,e,f).

A key feature of the latent-space DA system is that observation impact depends on the background state due to the decoder's nonlinearity (MZ24). We demonstrated this by repeating the same single-observation experiment on two different dates (Fig. 3).

So far, we have shown that horizontal balance in the midlatitudes is well preserved following a single observation assimilation, whereas in the vertical direction, the impact of the observation shows a maximum at the observed level

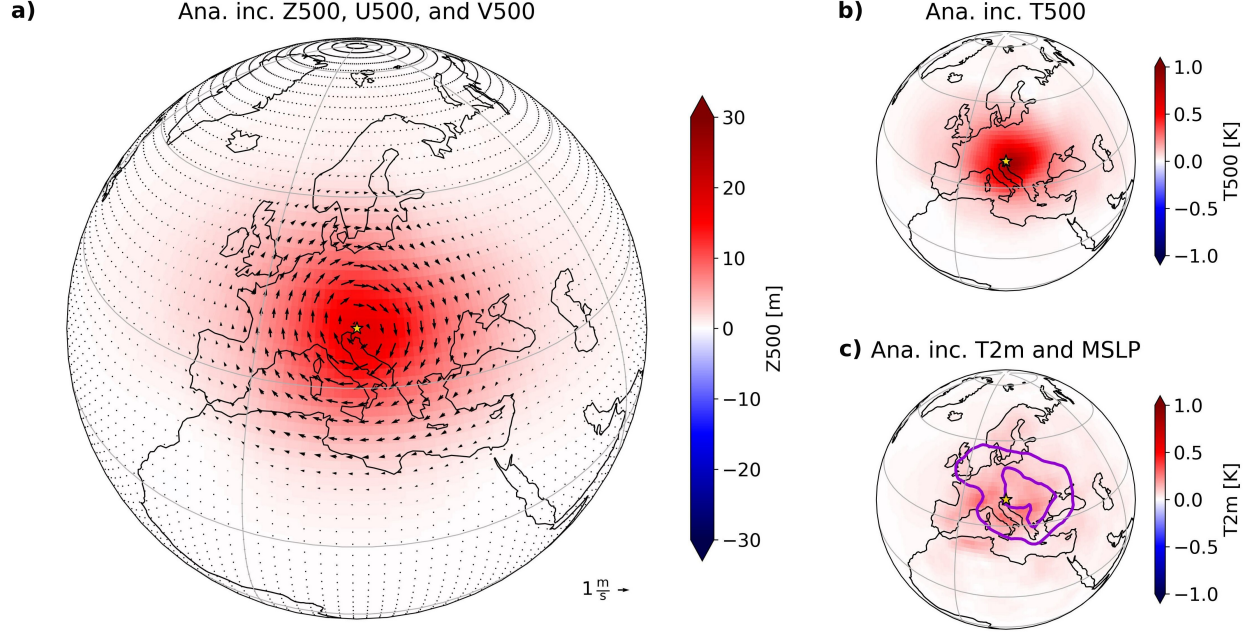


Figure 1: Analysis increments following an assimilation of Z500 observation above Ljubljana with departure of 30 m and observation-error standard deviation of 10 m. (a) Z500 increment (colors) and 500 hPa horizontal wind increment (arrows); (b) T500 increment; (c) T2m increment (colors) and MSLP increment (the two purple contours denote  $+0.15$  hPa, and  $+0.30$  hPa increments). The observation location is denoted by a golden star.

and gradually decreases both upward and downward. Another key physical constraint in this region is the thermal wind balance [Holton and Hakim, 2013], which links the vertical variation of horizontal wind to horizontal gradients in geopotential height, assuming geostrophic balance in the horizontal and hydrostatic balance in the vertical. Under these assumptions, the difference in analysis increments of zonal wind between 500 hPa and 700 hPa can be approximated by the thermal wind relation:

$$\delta_a^{U500} - \delta_a^{U700} \approx -\frac{g}{f} \frac{\partial(\delta_a^{Z500} - \delta_a^{Z700})}{\partial y}, \quad (6)$$

where  $g$  is acceleration due to gravity,  $f$  is the Coriolis parameter, and  $\partial/\partial y$  denotes the latitudinal derivative in units  $m^{-1}$ . Figure 4 confirms that this approximation holds well for the computed analysis increments, indicating that both the hydrostatic and the geostrophic balances are preserved after the assimilation.

Since no data assimilation algorithm is perfect, the resulting analysis is never fully consistent with the model's internal dynamics. Consequently, some information introduced by the analysis may introduce systematic biases, be dissipated during forward integration or lead to physically unrealistic forecasts [Kalnay, 2002]. Figure 5 illustrates the model's response to modified initial conditions from the single-observation experiment. Shown is the difference between two 48-hour forecasts initialized from the analysis and the background, respectively, for the same ensemble member.

A positive increment in Z500 at the initial time propagates eastward in line with the predominant Rossby wave phase speed (Fig. 5a,d,f), gradually also decreasing in magnitude. The increased anticyclonic vorticity also leads to increased advection of negative vorticity downstream, leading to enhanced cyclonic vorticity at 24-hour lead time east of the initial perturbation. To the southeast of the propagating signal, MSLP increases as expected, accompanied by a reduction in TCWV (Fig. 5e,h). This moisture reduction slightly lags a concurrent drop in T2m in the same region (Fig. 5f,i), collectively resembling the atmospheric response to a passing cold front. Overall, the primary information introduced by the analysis increment is retained throughout the 48-hour forecast integration.

### 3.2 Background error-covariance model in the tropics – a response to humidity saturation

The physical balances in the tropics vastly differ from those in the midlatitudes due to a much smaller Coriolis force and tend to be more complex to be described analytically. The primary energy source for atmospheric motions in the tropics is the latent heat release due to condensation in convective cloud systems which drives the large-scale tropical

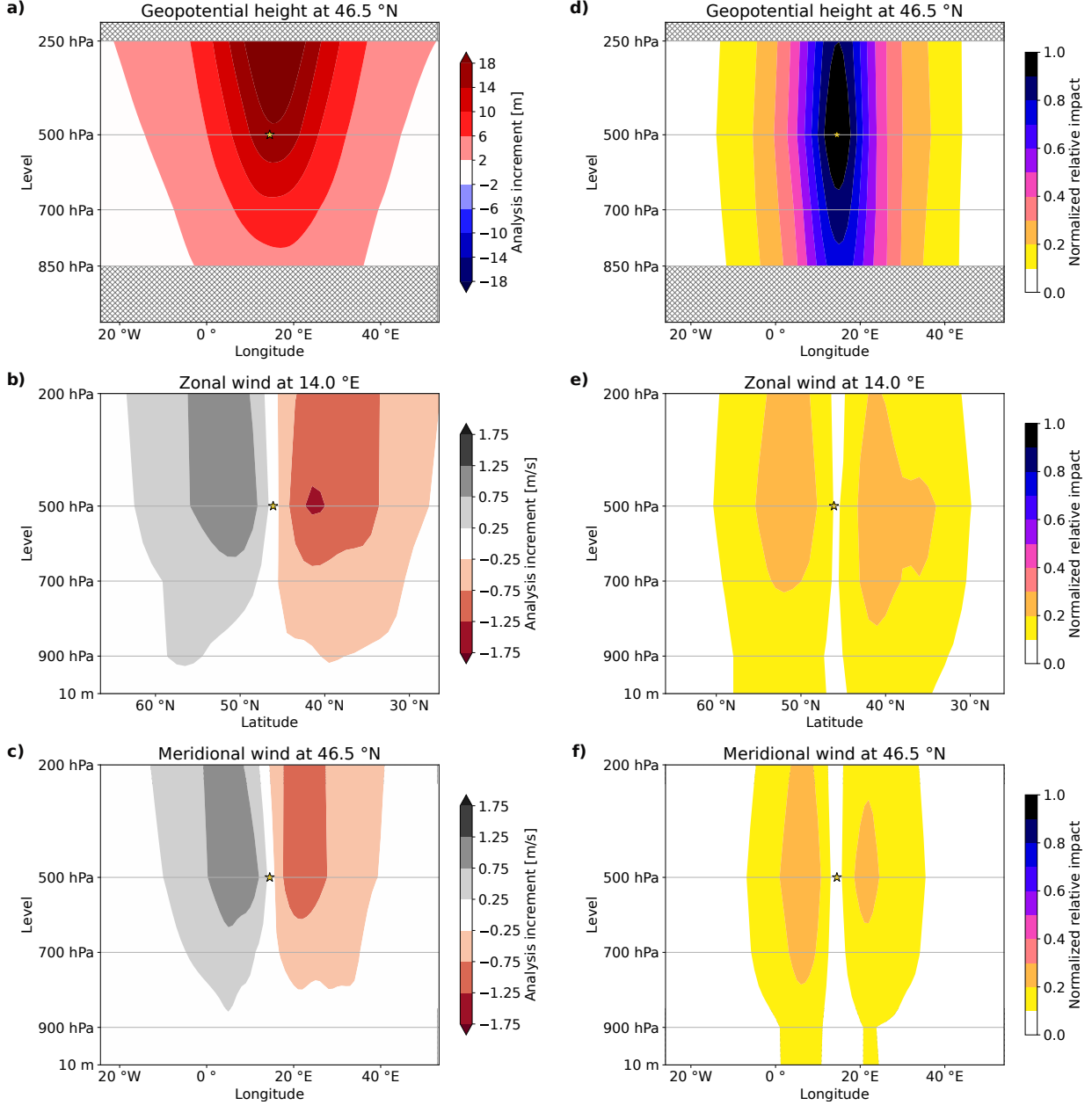


Figure 2: Vertical cross sections of analysis increments following an assimilation of Z500 observation. The cross section is done at the grid latitude or longitude nearest to the observation. (a) 2D longitude-pressure cross section of geopotential height increment at latitude  $46.5^{\circ}\text{N}$ . (b) 2D latitude-pressure cross section of zonal wind increment at longitude  $14.0^{\circ}\text{E}$ . (c) 2D latitude-pressure cross section of meridional wind at latitude  $46.5^{\circ}\text{N}$ . (d-f) As (a-c), but showing the normalized relative impact of the observation. Gaussian filtering with a standard deviation of  $1^{\circ}$  was applied in both horizontal directions to smoothen the contours. The observation location is denoted by a golden star.

circulation [Holton and Hakim, 2013]. Davey and Gill [1987] constructed a simplified analytical model to investigate how tropical atmospheric dynamics respond to latent heat sources. The diabatic heating in convective systems is balanced by the adiabatic cooling of ascending flow (updrafts) inside. This leads to a drop in the surface pressure below the perturbation, establishing a convergent horizontal wind pattern in the lower troposphere that can further fuel the development of a convective system. At the top of the convective system, the statically-stable tropopause acts as a lid for strong vertical motions, leading to the positive pressure perturbation and divergent horizontal outflow.

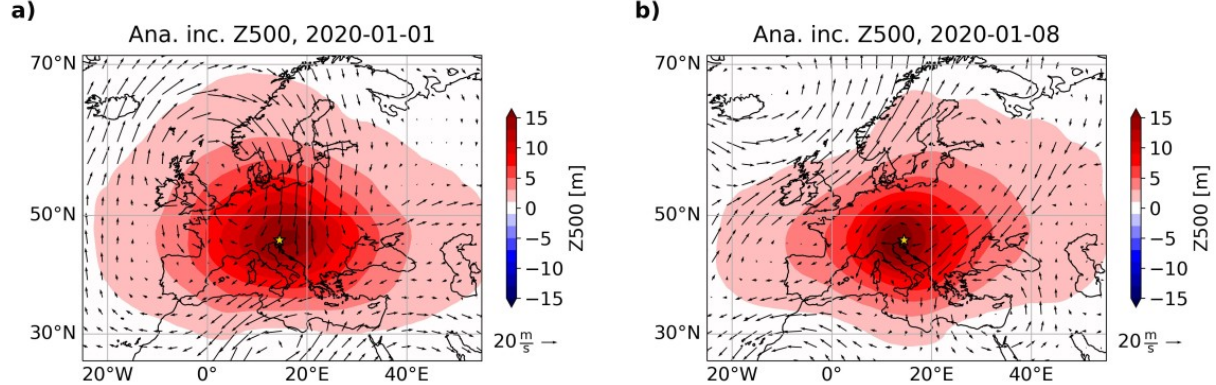


Figure 3: Z500 analysis increments following assimilation of Z500 observation above Ljubljana with 30 m departure and 10 m standard deviation on two different dates with different backgrounds: (a) January 1st, 2020, at 00 UTC, and (b) January 8th, 2020, at 00 UTC. The arrows denote the background 500 hPa wind. The observation location is marked by a golden star.

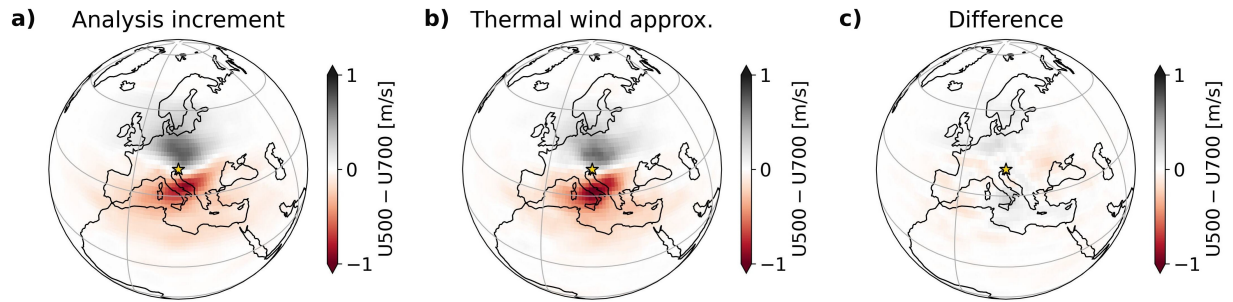


Figure 4: A comparison of (a) the difference in U500 and U700 analysis increments to (b) their difference derived from the thermal wind approximation in Eq. (6). (c) The difference ((a)–(b)).

Although our applied neural networks do not explicitly resolve clouds, condensation, latent heat release, or precipitation, they capture information on total column water vapour (TCWV) and its relationships with other atmospheric variables. We tested whether an increase in TCWV in a tropical area with high background TCWV leads to similar effects as described in Davey and Gill [1987] and obtained in simplified numerical studies of tropical response to latent heating [?]. Figure 6 shows the analysis increments following an assimilation of TCWV observation in the Central Atlantic Ocean (equator,  $33.0^{\circ}\text{W}$ ) with departure  $d^{\text{TCWV}} = 10 \text{ kg/m}^2$  and error standard deviation  $\sigma_o^{\text{TCWV}} = 3 \text{ kg/m}^2$ . The horizontal wind increments at 900 hPa (Fig. 6a) and 200 hPa (Fig. 6b) display convergence in the lower troposphere and divergence in the upper troposphere. At 900 hPa, we also observe a cyclonic vorticity pattern north/south of the perturbation. At 200 hPa, the wind increments are substantially stronger, and the latent-space DA system even generates a Kelvin wave east of the observation site. This highlights a remarkable capability of the latent-space background-error covariance model – one not yet demonstrated by any other system.

The analysis increment of TCWV (Fig. 6c) has an elliptic shape with a greater extent in the zonal than in the meridional direction, reflecting the dominance of the zonal flow in the tropical atmosphere. A negative increment in T2m is also present (Fig. 6d). This may indicate latent cooling due to evaporation of precipitation in the lowest layers – once again implicitly captured by the autoencoder.

Does our DA and the associated latent-space  $\mathbf{B}_z$ -matrix capture the response to latent-heat-induced perturbations in the tropics? To provide further evidence, we analyze the vertical profile of horizontal divergence in the analysis increment. Figure 6e shows that, at the location of the observed TCWV, the convergent wind increment is present in the lower troposphere, peaking around 900 hPa. Near 500 hPa, the flow transitions to divergent, which peaks at 200 hPa, with a magnitude twice as large as the maximum convergence. This structure closely resembles observational findings from Williams and Gray [1973], suggesting that our system realistically represents the dynamical response to tropical latent heating.

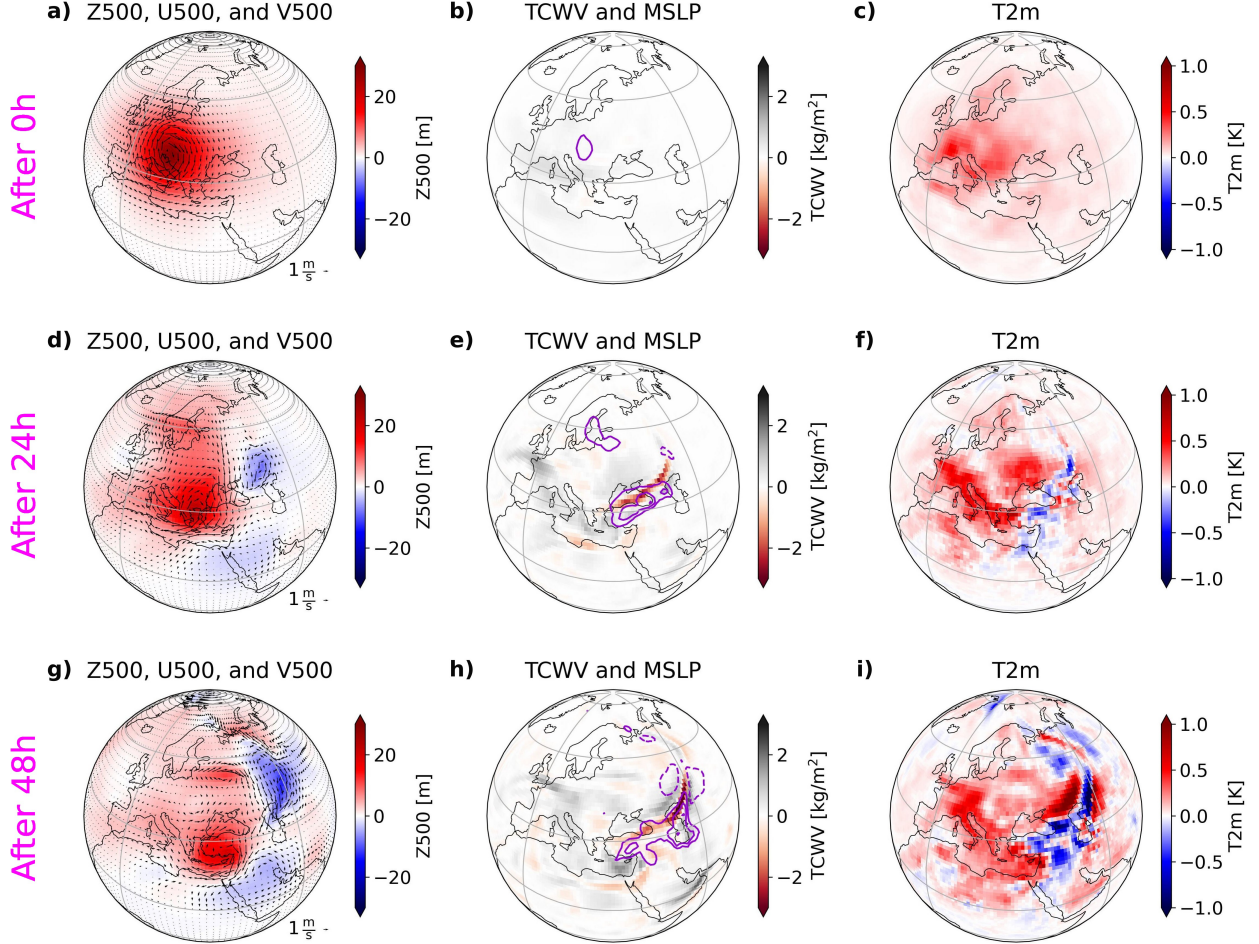


Figure 5: Difference between the two forecasts initialized from the analysis and the background, respectively, for a selected ensemble member, based on the experiment in Fig. 1. Difference in the initial condition (the analysis increment) for (a) Z500 (colors) and 500 hPa wind (arrows), (b) total-column water vapor (colors) and MSLP (purple contours), and (c) T2m. (d-f) As (a-c), but for the 24-hour forecast lead time. (g-i) As (d-f), but for the 48-hour forecast lead time. The solid/dashed contours in (b,e,h) indicate a positive/negative difference with 0.5 hPa step, zero contour is omitted.

Similarly to Fig. 5, Figure 7 illustrates the model's response to the initial perturbation introduced in the tropical single-observation experiment. The TCWV increment is advected westwards with the background 900 hPa wind (note that the 900 hPa wind increment in Fig. 7b,d,f,h is negligible compared to the background shown in Fig. 7a,c,e,g). Since specific humidity decreases exponentially with height [?], the TCWV advection is primarily governed by the lower-tropospheric winds. This behavior reaffirms the physical realism of the learned neural-network dynamics. The positive TCWV increment disperses before reaching the coast of Brazil. Meanwhile, the 900 hPa wind and MSLP increments (Fig. 7b,d,f) reveal the development of an eastward travelling Kelvin wave, which is fully developed by 48 hours (Fig. 7h).

#### 4 Estimating latent space background-error covariance model from operational EDA

So far, we have shown that latent-space DA, using a climatological  $B_z$ -matrix, produces physically reasonable analysis increments both in the tropics and midlatitudes. In this section, we extend our approach by incorporating the ensemble of data assimilation (EDA, Isaksen et al. [2010]), to capture fully flow-dependent background-error variances, commonly referred to as "the errors of the day" [Bonavita et al., 2012].

We used an ensemble of backgrounds, valid on April 14th, 2024, at 00 UTC, from ECMWF's IFS cycle 49r1 [ECMWF, 2024], to derive flow-dependent background-error covariances in the latent space. The ensemble-derived background-

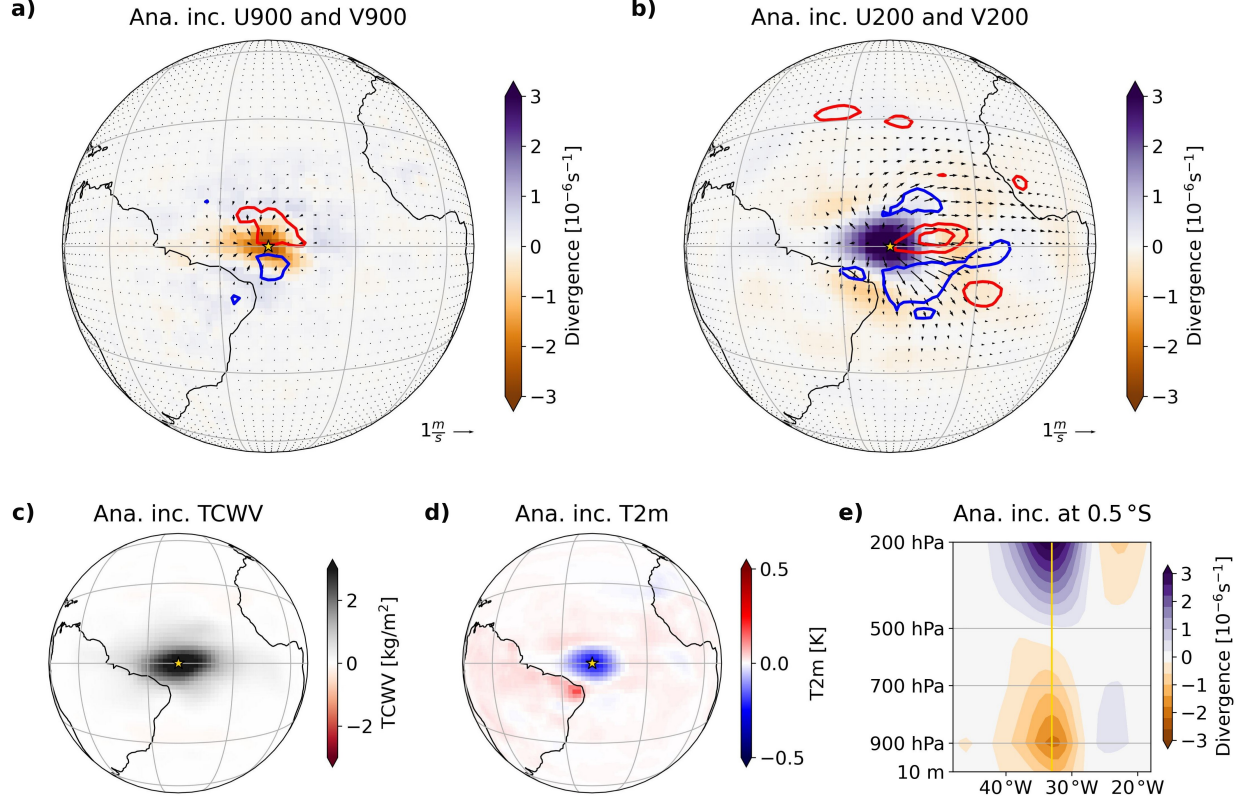


Figure 6: Analysis increments following an assimilation of TCWV observation above Central Atlantic with  $10 \text{ kg/m}^2$  departure and  $3 \text{ kg/m}^2$  observation-error standard deviation. (a) 900 hPa horizontal wind increment (arrows), its divergence (colors) and vorticity (contours); (b) as (a) but at 200 hPa; (c) TCWV increment; (d) T2m increment; (e) 2D longitude-pressure cross section of divergence of the wind increments at the observation location ( $0.5^\circ \text{S}$ ). The vertical line corresponds to the longitude of the observed TCWV. Red/blue vorticity contours in (a,b) correspond to positive/negative vorticity with a step of  $5 \times 10^{-7} \text{ s}^{-1}$ , zero-contour is omitted. Horizontal smoothing of the contours in panel (e) was applied as in Fig. 2.

error covariance matrix was computed as

$$\mathbf{B}_z^{\text{EDA}} = \frac{1}{N-1} \sum_{i=1}^N \left( \mathbf{z}_{b,i}^{\text{IFS}} - \langle \mathbf{z}_b^{\text{IFS}} \rangle \right) \left( \mathbf{z}_{b,i}^{\text{IFS}} - \langle \mathbf{z}_b^{\text{IFS}} \rangle \right)^\top, \quad (7)$$

where  $N = 50$  is the total number of ensemble members,  $\mathbf{z}_{b,i}^{\text{IFS}} = E \circ S(\mathbf{x}_{b,i}^{\text{IFS}})$  is an encoded ensemble member with index  $i$ , and  $\langle \mathbf{z}_b^{\text{IFS}} \rangle = \frac{1}{N} \sum_{i=1}^N E \circ S(\mathbf{x}_{b,i}^{\text{IFS}})$  is the ensemble mean of the encoded vectors. Figure C5 shows that the latent-space variances (diagonal elements) typically exceed the covariances (off-diagonal elements) by an order of magnitude. However, this contrast is less pronounced than in the climatological  $\mathbf{B}_z$  (Fig. C3b), which makes neglecting off-diagonal elements in 3D-Var minimization less justifiable. However, the off-diagonals span a similar range in both matrices, which may suggest they primarily reflect sampling noise.

Climatology-based background-error variances tend to overestimate forecast uncertainty [Bannister, 2008a], whereas ensemble-derived variances often underestimate it. Consequently, ensemble-derived variances are typically smaller than the climatological variability in the AE training set, potentially limiting AE's ability to reproduce such variances accurately. Additionally, neural networks are known to smooth meteorological fields [Bonavita, 2023], reducing their capacity to reconstruct the smallest-scale features in the ensemble after encoding and decoding. The vast difference in variability is evident in Fig. C6, where rows A and C show that the variances (represented by the standard deviation at each grid point) from the operational ensemble are approximately an order of magnitude smaller than those generated using  $\mathbf{B}_z^{\text{clim}}$  (see Fig. C4, rows C and H). Rows B and D of Fig. C6 display the standard deviation of the 50 ensemble members after processing through the AE. As expected, fine-scale details are lost due to the AE's limited resolution.

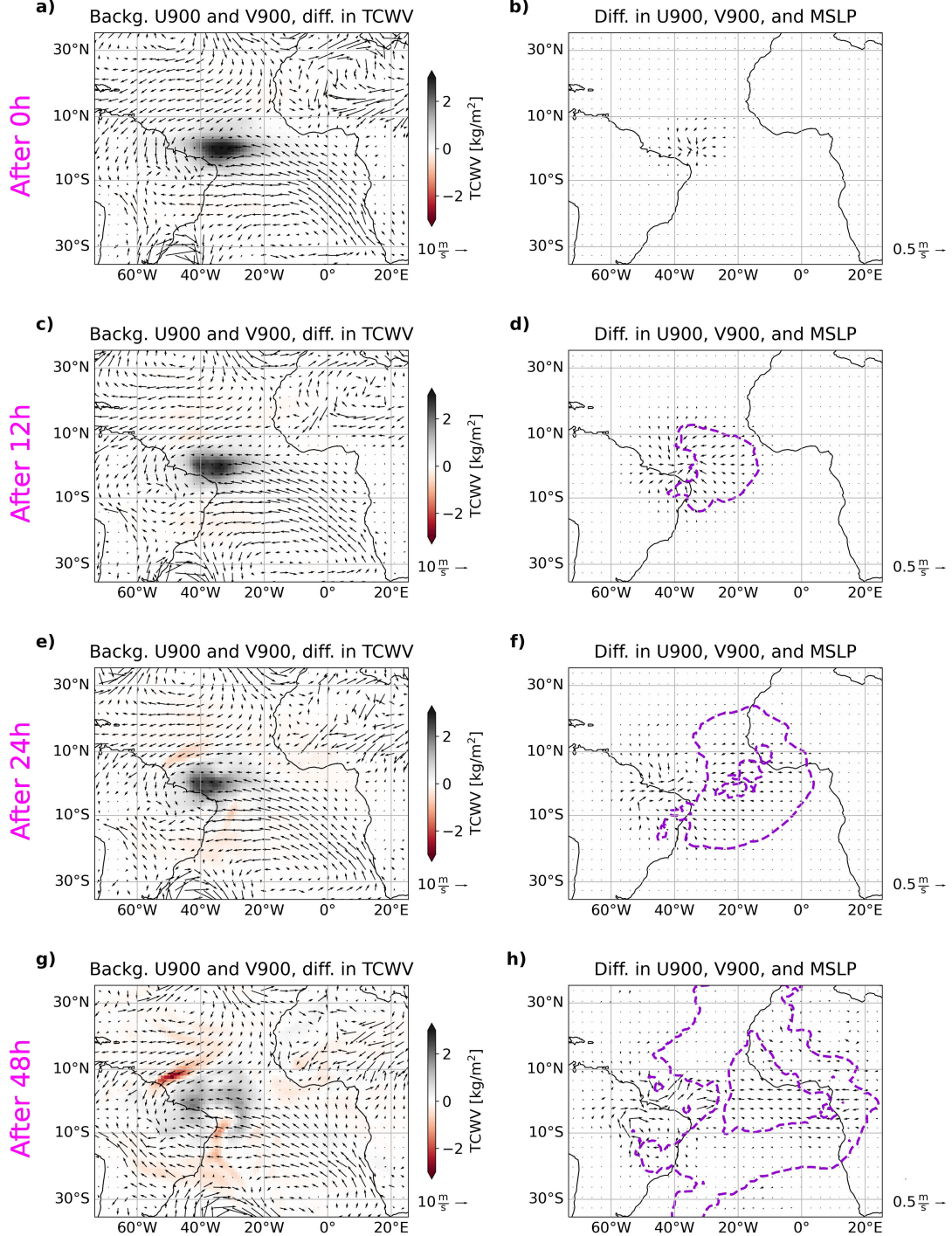


Figure 7: Difference between the two forecasts initialized from the analysis and the background, respectively, for a selected ensemble member, based on the experiment in Fig. 6. (a) Difference in the initial condition for TCWV (colors) on top of the 900 hPa background wind (arrows). (b) Difference in the initial condition for the 900 hPa wind (arrows; there is an order of magnitude difference in wind magnitude scaling compared to panel (a)). (c-d) As (a-b), but for the 12-hour forecast lead time. (e-f) As (a-b), but for the 24-hour forecast lead time. (g-h) As (a-b), but for the 48-hour forecast lead time.. The dashed contours in (d,f,h) indicate a negative MSLP difference with 0.1 hPa step, zero contour is omitted.

Nevertheless, ensemble variability remains reasonably well preserved for the geopotential height fields, which includes less variance in the small scales. In contrast, it is poorly reconstructed for other fields – particularly wind components, which have more variance in the small scales.

Using an ensemble of encoded backgrounds and EDA-derived background-error covariance matrix, we repeated a single observation experiment with  $d^{Z500} = 30 \text{ m/s}$  and  $\sigma_o^{Z500} = 10 \text{ m/s}$  over Ljubljana in Fig. 8a,c-e revealed that the resulting analysis increment preserved the geostrophic and thermal wind balance. To study the effect of the  $\mathbf{B}_z$ -matrix on the increment, we repeated the experiment once more using the ensemble of backgrounds, but applied  $\mathbf{B}_z^{clim}$  for 3D-Var cost function computation (Fig. 8b). Aside from a significantly stronger analysis increment magnitude (approximately five times larger at the observation location) and standard deviation (fourfold increase; not shown), both of which are expected due to an order of magnitude difference in the latent-space variances between the respective  $\mathbf{B}_z$  matrices, the analysis increments exhibit only minor qualitative differences.

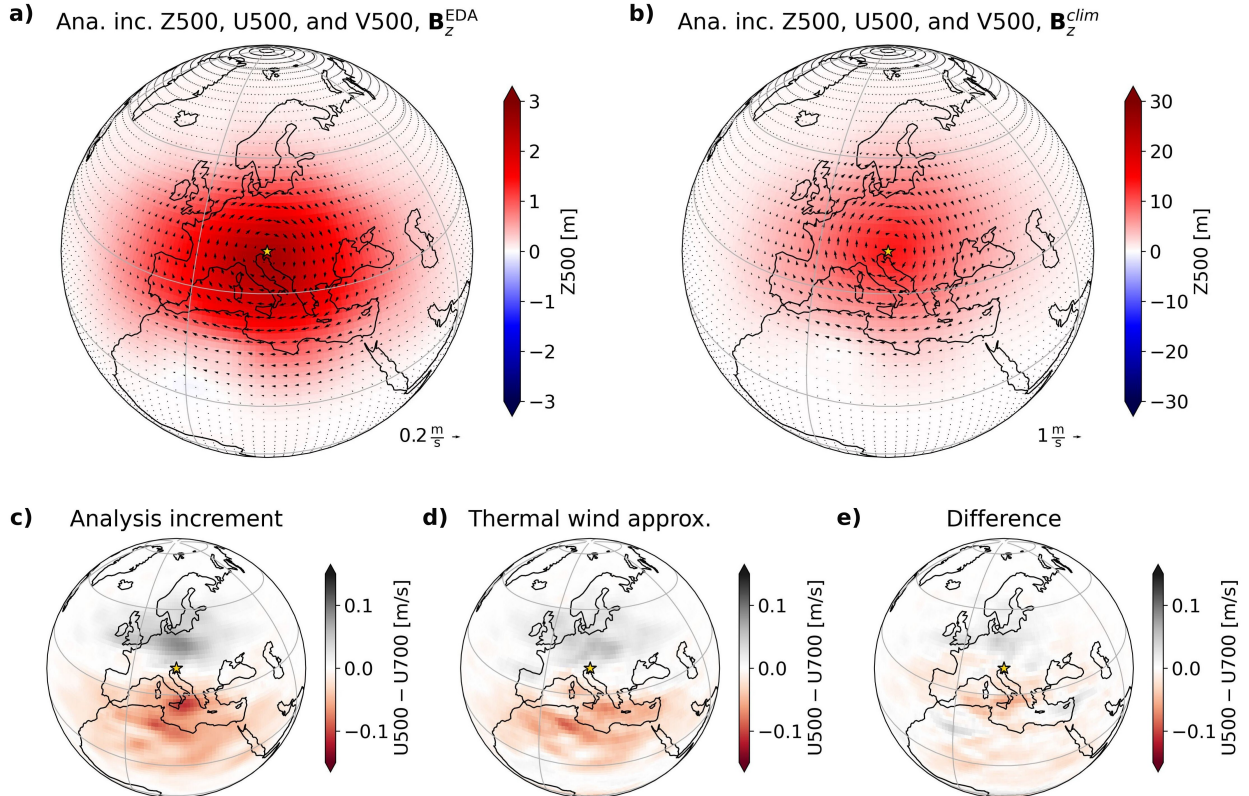


Figure 8: (a,b) As Fig. 1a but for an experiment using an operational EDA ensemble of backgrounds and (a) its corresponding  $\mathbf{B}_z$ -matrix and (b) climatological  $\mathbf{B}_z$ -matrix from Eq. (3). Note the different color and arrow scales in panel (a) compared to Fig. 1a and Fig. 8b. (c-e) As Fig. 4a-c, but computed for the experiment from panel (a).

Beyond the differences in the physical space, the analysis increments also differ in the latent space. Figure 9 presents histograms of the relative changes in latent vector elements following 3D-Var cost function minimization across four different experiments. These histograms reveal that, in each experiment, only a small fraction of 12100 elements undergo substantial modification. In the three experiments involving single Z500 observation, the same subset of latent elements is consistently among the most modified, and these changes predominantly affect the region where the analysis increment peaks (Fig. C7). In contrast, these elements are negligibly modified when observing TCWV in the Central Atlantic, where the most adjusted latent element mainly alters the region in the vicinity of that observation (Fig. 9d, Fig. C7, row J).

The most important benefit of using operational forecast ensembles in DA is their ability to provide flow-dependent background-error variances. Fan et al. [2025] demonstrated that even when using a static, climatology-based  $\mathbf{B}_z$ -matrix (in their case computed via the NMC method), latent DA can still produce covariances in the physical space that reflect the background state, and we reaffirmed that in Fig. 3. Losing this capability when transitioning from  $\mathbf{B}_z^{clim}$  to an ensemble-derived  $\mathbf{B}_z^{EDA}$  would represent a major drawback and would strongly undermine the motivation for making

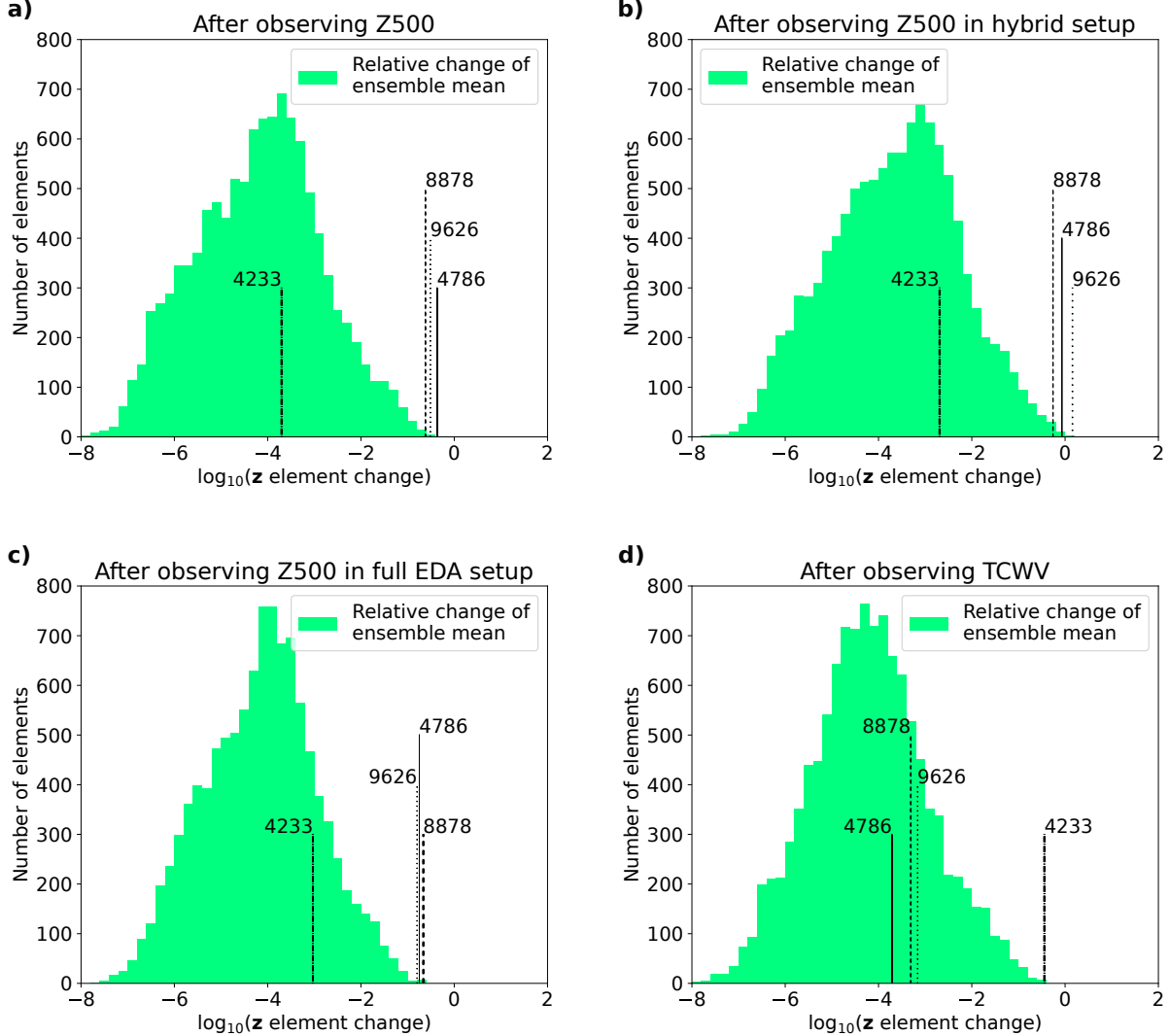


Figure 9: Histograms of the relative change of respective ensemble members in different experiments. The relative change is calculated as the difference of the latent element's ensemble mean before and after the assimilation divided by the latent element's analysis standard deviation. The indices of the most altered element in each of the experiments are highlighted in all four plots. (a) The histogram for the experiment with observing Z500 above Ljubljana using the original setup (Sec. 3.1). (b) The histogram for the experiment with observing Z500 above Ljubljana using IFS ensemble forecast as the background and climatological  $B_z$  in 3D-Var cost function minimization. (c) The histogram for the experiment with observing Z500 above Ljubljana using IFS ensemble forecast as the background and its proper  $B_z$  in 3D-Var cost function. (d) The histogram for the experiment with observing TCWV above Central Atlantic using the original setup (Sec. 3.2). The bin width is 0.2 on a logarithmic scale.

such a change. Similarly to Figure 3, Figure 10 illustrates two examples of the impact of a single Z500 observation above Ljubljana, but using the same ensemble of background states in both cases and different  $B_z$ -matrices. While it is difficult to determine which spread of the information from the observation more faithfully follows the background flow, both retain some flow-dependent structure. This indicates that switching from  $B_z^{clim}$  to  $B_z^{EDA}$  does not degrade the method's ability to represent flow-dependent features. However, given the current performance of the AE, it also does not lead to substantial improvements.

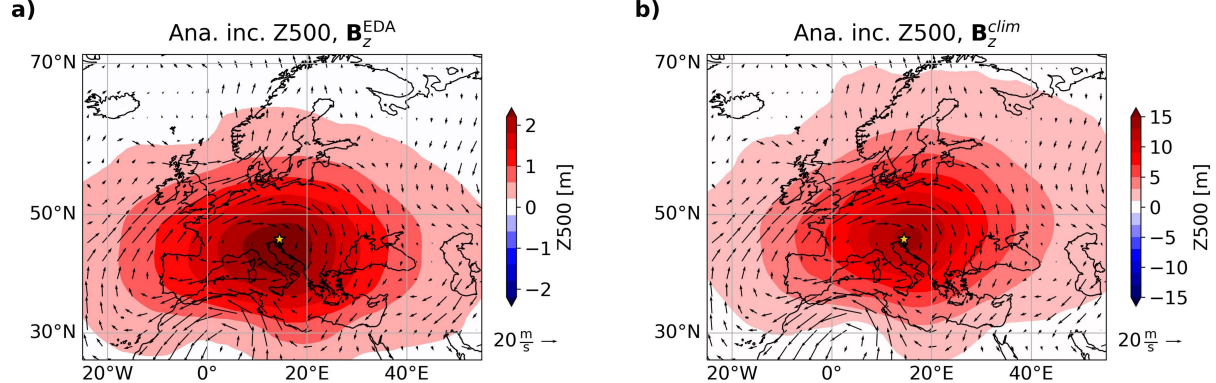


Figure 10: As Fig. 3, but using the encoded IFS ensemble as the background and (a)  $\mathbf{B}_z^{\text{EDA}}$  or (b)  $\mathbf{B}_z^{\text{clim}}$  in 3D-Var cost function computation.

## 5 Discussion, conclusion, and outlook

The motivation for this study was to advance the representation of background-error covariances for variational data assimilation (DA) to better capture both tropical and extratropical balances. Although several analytical approaches have been proposed to address this challenge [Žagar et al., 2004, Körnich and Källén, 2008], none have been implemented in operational systems. Therefore, they still lack multivariate representation of tropical background-error covariances, including the balance structures. To address this gap, we explored an alternative approach by computing covariances in the reduced-dimension latent space, learned by a convolutional autoencoder, and reformulating the 3D-Var cost function to be minimized within that space. This method has already shown promising results in a univariate context (MZ24), and has been demonstrated to produce analysis increments in the midlatitudes that exhibit both geostrophic horizontal structure and flow-dependent characteristics [Fan et al., 2025]. In the present study, we extended the approach in MZ24 to multivariate, multilevel representation of the atmosphere, and tested the physical plausibility of the resulting analysis increments through single-observation data assimilation experiments.

Using a climatology-based background-error covariance matrix computed as a difference between 24-hour neural network forecast and the corresponding ground truth, we showed that an observation of 500 hPa geopotential height (Z500) produces an analysis increment with a geostrophically balanced pattern in both 500-hPa geopotential height and winds (Fig. 1a). The observational information is also realistically propagated vertically and across variables (Figs. 1b,c, 2). Moreover, the analysis increment preserves the thermal wind balance (Fig. 4), indicating that both geostrophic and hydrostatic balance are preserved during the assimilation process. In the tropics, an assimilation of a single total column water vapor (TCWV) observation with positive departure in an atmosphere near saturation led to an analysis increment consistent with the theoretical dynamical response to heat-induced perturbations (Fig. 6), resulting in convergent winds in the lower troposphere and divergent winds aloft. This happened, despite the humidity, convection, and precipitation not being explicitly represented in the applied neural networks. Forecasts initialized from the resulting analyses produced physically plausible weather evolution: in the midlatitudes, a developing cold front (Fig. 5); and in the tropics, a propagating Kelvin wave and a TCWV structure advected by lower-tropospheric winds (Fig. 7).

A key difference between the analysis increments in this study and those presented in MZ24 lies in their horizontal extent – here, the increments are significantly more localized, particularly in the tropics. We found that perturbing individual elements of the latent vector leads to localized changes in the decoded atmospheric fields (Fig. C7). During assimilation, the algorithm primarily adjusted those latent vector elements that describe the features near the observation location (Figs. 9, C7). This represents a substantial improvement in the applicability of the approach: in MZ24, perturbations to individual latent vector elements resulted in global changes to the decoded fields. This improvement is likely due to the use of a higher-quality autoencoder in the present study, featuring a latent space two orders of magnitude larger than that of MZ24. Incorporating neural networks with even greater representational capacity and larger latent spaces could further enhance localization and provide a more diverse set of learned weather patterns within the latent space.

This approach may also be promising to describe background-error cross-covariances between atmosphere, ocean, and land, as well as for the assimilation of land, ocean or even hydrological observations, potentially offering a unified framework for these traditionally complex and distinct assimilation procedures [Park and Xu, 2009]. While Zheng et al. [2024] applied a similar method to assimilate sea surface temperature over the Pacific, we tried to explore the effect of observing surface temperature (ST) on nearby locations over land and ocean on the local vertical temperature profile

(not shown). However, we were unable to detect any substantial differences. We speculate that this is due to limitations in the reconstruction quality of our NNs, and possibly also due to their coarse vertical resolution of temperature fields. In general, we can conclude that the  $\mathbf{B}_z$ -matrix realistically captures the contrast in ST variance between land and sea (Fig. C4, panel C6), and that the assimilation procedure yields distinct responses in ST and 2-meter temperature (T2m). For example, after assimilating Z500 over Ljubljana, the impact on T2m is approximately twice that on ST (Fig. C4, panels E6-7). Similarly, following the introduction of a positive TCWV departure over the central Atlantic, a local negative increment appears in T2m (Fig. 6d), while the ST increment shows no discernible pattern.

Another challenge addressed in this study was the transition from climatology-based to ensemble-based background error covariance matrices. Despite a substantial loss of ensemble variance information after encoding the ensemble of backgrounds from operational EDA of ECMWF (Fig. C6) – caused by both limitations in the autoencoder’s representational capacity, the analysis increment obtained after assimilating Z500 in the midlatitudes still respected both horizontal and vertical physical balances. Importantly, the increment’s flow-dependent characteristics were retained (Fig. 10). In the long term, using ensemble-derived background error covariances holds promise for capturing even more flow-dependent features and for estimating covariance magnitudes more accurately than with climatology-based matrices. However, a successful use of that approach is not self evident as the AE was trained on decades of reanalysis data, which made it capable of catching various weather patterns within the atmosphere’s climatology.

As in previous studies on latent-space DA for meteorological applications [MZ24, Zheng et al., 2024, Fan et al., 2025], we used only the diagonal elements of the background-error covariance matrix in the 3D-Var cost function. While we did not conclusively demonstrate that the off-diagonal terms have a negligible impact, the results show that the increments produced using only the diagonal terms thoroughly respect physical balances across both types of  $\mathbf{B}_z$  matrices tested. As emphasized throughout this discussion, the assimilation approach would likely benefit from higher-capacity neural networks, but these would require even larger latent spaces, making the quasi-diagonality assumption for  $\mathbf{B}_z$  practically necessary. Meanwhile, potential challenges stemming from non-Gaussianity in the latent space could be mitigated using techniques such as normalizing flows, as proposed by Böhm and Seljak [2022].

Overall, this method has demonstrated the ability to generate physically consistent, flow-dependent analysis increments in both tropical and extratropical atmosphere, all while maintaining relatively low computational cost. Given its promising performance with ensemble-derived background-error covariances and the physical realism of forecasts initialized from the resulting analyses, we believe this approach could be further extended towards a full ensemble-based latent-space 4D-Var system, comparable to those used in operational weather forecasting centers.

## Acknowledgements

This research was funded by Slovenian Research and Innovation Agency (ARIS) Programme P1-0188 and Grant MR-56969. This research was also supported by the University of Ljubljana Grant SN-ZRD/22-27/0510. Žiga Zaplotnik acknowledges the funding by the European Union under the Destination Earth initiative. The authors are grateful to Nedeljka Žagar (Universität Hamburg) and Massimo Bonavita (ECMWF) for fruitful discussions on the topic.

## References

- G. Andry, F. Rozet, S. Lewin, O. Rochman, V. Mangeleer, M. Pirlet, E. Faulx, M. Grégoire, and G. Louppe. Appa: Bending Weather Dynamics with Latent Diffusion Models for Global Data Assimilation. *Arxiv preprint*, 2025. doi: 10.48550/arXiv.2504.18720.
- R. N. Bannister. A review of forecast error covariance statistics in atmospheric variational data assimilation. I: Characteristics and measurements of forecast error covariances. *Quarterly Journal of the Royal Meteorological Society*, 134(637):1951–1970, 2008a. ISSN 00359009. doi: 10.1002/qj.339.
- R. N. Bannister. A review of forecast error covariance statistics in atmospheric variational data assimilation. II: Modelling the forecast error covariance statistics. *Quarterly Journal of the Royal Meteorological Society*, 134(637):1971–1996, 2008b. ISSN 00359009. doi: 10.1002/qj.340.
- V. Böhm and U. Seljak. Probabilistic Autoencoder. *Trans. Mach. Learn. Res.*, 2022, 9 2022. URL <https://openreview.net/forum?id=AEoYjvjKVA>.
- M. Bonavita. On some limitations of data-driven weather forecasting models. *Arxiv preprint*, 2023. doi: 10.48550/arXiv.2309.08473.
- M. Bonavita, L. Isaksen, and E. Hólm. On the use of EDA background error variances in the ECMWF 4D-Var. *Quarterly Journal of the Royal Meteorological Society*, 138(667):1540–1559, 2 2012. ISSN 00359009. doi: 10.1002/qj.1899.

- K. Chen, L. Bai, F. Ling, P. Ye, T. Chen, J.-J. Luo, H. Chen, Y. Xiao, K. Chen, T. Han, and W. Ouyang. Towards an end-to-end artificial intelligence driven global weather forecasting system. *Arxiv preprint*, 2023. doi: 10.48550/arXiv.2312.12462.
- K. Chen, P. Ye, H. Chen, K. Chen, T. Han, W. Ouyang, T. Chen, and L. Bai. FNP: Fourier Neural Processes for Arbitrary-Resolution Data Assimilation. In *38th Conference on Neural Information Processing Systems*, 2024. URL <https://openreview.net/pdf?id=4rrNcsVPDm>.
- S. Cheng, C. Quilodran-Casas, S. Ouala, A. Farchi, C. Liu, P. Tandeo, R. Fablet, D. Lucor, B. Iooss, J. Brajard, D. Xiao, T. Janjic, W. Ding, Y. Guo, A. Carrassi, M. Bocquet, and R. Arcucci. Machine Learning With Data Assimilation and Uncertainty Quantification for Dynamical Systems: A Review. *IEEE/CAA Journal of Automatica Sinica*, 10(6):1361–1387, 2 2023. ISSN 23299274. doi: 10.1109/JAS.2023.123537.
- Copernicus Climate Change Service Climate Data Store. ERA5 hourly data on single levels from 1940 to present, 2023.
- M. K. Davey and A. E. Gill. Experiments On Tropical Circulation With A Simple Moist Model. *Quarterly Journal of the Royal Meteorological Society*, 113(478):1237–1269, 10 1987. ISSN 0035-9009. doi: 10.1002/qj.49711347809.
- ECMWF. IFS Documentation CY49R1 - Part II: Data Assimilation. In *IFS Documentation CY49R1*, pages 1–108. European Centre for Medium-Range Weather Forecasts Shinfield Park, Reading, RG2 9AX, UK, 2024. doi: 10.21957/105cb1333c.
- H. Fan, B. Fei, P. Gentine, Y. Xiao, K. Chen, Y. Liu, Y. Qu, F. Ling, and L. Bai. Physically Consistent Global Atmospheric Data Assimilation with Machine Learning in a Latent Space. *Arxiv preprint*, 2 2025. doi: 10.48550/arXiv.2502.02884.
- H. Hersbach, B. Bell, P. Berrisford, S. Hirahara, A. Horányi, J. Muñoz-Sabater, J. Nicolas, C. Peubey, R. Radu, D. Schepers, A. Simmons, C. Soci, S. Abdalla, X. Abellán, G. Balsamo, P. Bechtold, G. Biavati, J. Bidlot, M. Bonavita, G. De Chiara, P. Dahlgren, D. Dee, M. Diamantakis, R. Dragani, J. Flemming, R. Forbes, M. Fuentes, A. Geer, L. Haimberger, S. Healy, R. J. Hogan, E. Hólm, M. Janisková, S. Keeley, P. Laloyaux, P. Lopez, C. Lupu, G. Radnoti, P. de Rosnay, I. Rozum, F. Vamborg, S. Villaume, and J. Thépaut. The ERA5 global reanalysis. *Quarterly Journal of the Royal Meteorological Society*, 146(730):1999–2049, 2020. ISSN 0035-9009. doi: 10.1002/qj.3803.
- J. R. Holton and G. J. Hakim. *An Introduction to Dynamic Meteorology*. Academic Press, fifth edition, 2013. ISBN 978-0-12-384866-6.
- L. Isaksen, M. Bonavita, R. Buizza, M. Fisher, J. Haseler, M. Leutbecher, and L. Raynaud. Ensemble of Data Assimilations at ECMWF, 2010. URL <http://www.ecmwf.int/publications/>.
- E. Kalnay. *Atmospheric Modeling, Data Assimilation and Predictability*. Cambridge University Press, 2002. ISBN 978-0-521-79179-3.
- A. Kasahara and K. Puri. Spectral Representation of Three-Dimensional Global Data by Expansion in Normal Mode Functions. *Monthly Weather Review*, 109(1):37–51, 1981. ISSN 0027-0644. doi: 10.1175/1520-0493(1981)109<0037:SROTDG>2.0.CO;2.
- H. Körnich and E. Källén. Combining the mid-latitudinal and equatorial mass/wind balance relationships in global data assimilation. *Tellus A: Dynamic Meteorology and Oceanography*, 60(2):261–272, 2008. ISSN 1600-0870. doi: 10.1111/j.1600-0870.2007.00286.x.
- W. Lahoz, B. Khattatov, and R. Ménard, editors. *Data assimilation: Making sense of observations*. Springer Berlin Heidelberg, 2010. ISBN 9783540747024. doi: 10.1007/978-3-540-74703-1.
- Y. Li, W. Han, H. Li, W. Duan, L. Chen, X. Zhong, J. Wang, Y. Liu, and X. Sun. FuXi-En4DVar: An Assimilation System Based on Machine Learning Weather Forecasting Model Ensuring Physical Constraints. *Geophysical Research Letters*, 51(22), 2024. ISSN 0094-8276. doi: 10.1029/2024GL111136.
- T. Matsuno. Quasi-Geostrophic Motions in the Equatorial Area. *Journal of the Meteorological Society of Japan*, 44(1):25–43, 1966. doi: 10.2151/jmsj1965.44.1{\\_}25.
- B. Melinc and Z. Zaplotnik. 3D-Var data assimilation using a variational autoencoder. *Quarterly Journal of the Royal Meteorological Society*, 150(761):2273–2295, 2 2024. ISSN 1477870X. doi: 10.1002/qj.4708.
- S. K. Park and L. Xu, editors. *Data Assimilation for Atmospheric, Oceanic and Hydrologic Applications*. Springer Berlin Heidelberg, Berlin, Heidelberg, 2009. ISBN 978-3-540-71055-4. doi: 10.1007/978-3-540-71056-1.
- I. Pasman, Y. Chen, T. S. Finn, M. Bocquet, and A. Carrassi. Ensemble Kalman filter in latent space using a variational autoencoder pair. *Arxiv preprint*, 2025. doi: 10.48550/arXiv.2502.12987.
- U. Perkan, Z. Zaplotnik, and G. Skok. Using gridpoint relaxation for forecast error diagnostics in neural weather models. *Article in preparation.*, 2025.
- O. Ronneberger, P. Fischer, and T. Brox. U-Net: Convolutional Networks for Biomedical Image Segmentation. *Arxiv preprint*, 2015. doi: 10.48550/arXiv.1505.04597.

- X. Sun, X. Zhong, X. Xu, Y. Huang, H. Li, J. D. Neelin, D. Chen, J. Feng, W. Han, L. Wu, and Y. Qi. FuXi Weather: A data-to-forecast machine learning system for global weather. *Arxiv preprint*, 2 2024. doi: 10.48550/arXiv.2408.05472.
- K. T. Williams and W. M. Gray. Statistical analysis of satellite-observed trade wind cloud clusters in the western North Pacific. *Tellus*, 25(4):313–336, 8 1973. ISSN 00402826. doi: 10.1111/j.2153-3490.1973.tb00617.x.
- Y. Xiang, W. Jin, H. Dong, M. Bai, Z. Fang, P. Zhao, H. Sun, K. Thambiratnam, Q. Zhang, and X. Huang. ADAF: An Artificial Intelligence Data Assimilation Framework for Weather Forecasting. *Arxiv preprint*, 2024. doi: 10.48550/arXiv.2411.16807.
- Y. Xiao, L. Bai, W. Xue, K. Chen, T. Han, and W. Ouyang. FengWu-4DVar: Coupling the Data-driven Weather Forecasting Model with 4D Variational Assimilation. *Arxiv preprint*, 2 2023. doi: 10.48550/arXiv.2312.12455.
- X. Xu, X. Sun, W. Han, X. Zhong, L. Chen, Z. Gao, and H. Li. FuXi-DA: a generalized deep learning data assimilation framework for assimilating satellite observations. *npj Climate and Atmospheric Science*, 8(1):156, 2025. ISSN 2397-3722. doi: 10.1038/s41612-025-01039-3.
- N. Žagar, N. Gustafsson, and E. Källén. Variational data assimilation in the tropics: The impact of a background-error constraint. *Quarterly Journal of the Royal Meteorological Society*, 130(596):103–125, 2004. ISSN 0035-9009. doi: 10.1256/qj.03.13.
- N. Žagar, E. Andersson, and M. Fisher. Balanced tropical data assimilation based on a study of equatorial waves in ECMWF short-range forecast errors. *Quarterly Journal of the Royal Meteorological Society*, 131(607):987–1011, 2005. ISSN 00359009. doi: 10.1256/qj.04.54.
- N. Žagar, L. Isaksen, D. Tan, and J. Tribbia. Balance properties of the short-range forecast errors in the ECMWF 4D-Var ensemble. *Quarterly Journal of the Royal Meteorological Society*, 139(674):1229–1238, 2013. ISSN 0035-9009. doi: 10.1002/qj.2033.
- Q. Zheng, G. Han, W. Li, L. Cao, G. Zhou, H. Wu, Q. Shao, R. Wang, X. Wu, X. Cui, H. Li, and X. Wang. Generating Unseen Nonlinear Evolution in Sea Surface Temperature Using a Deep Learning-Based Latent Space Data Assimilation Framework. *Arxiv preprint*, 2024. doi: 10.48550/arXiv.2412.13477.

## A Appendix A: Neural network design

### A.1 Autoencoder

The structure of the autoencoder (AE), illustrated in Fig. A1, consists of the encoder and the decoder. The encoder  $E$  comprises four convolutional blocks, each containing four subblocks with a consistent design. In each block, the input field is first padded using spherical padding, which is periodic in the zonal direction and polar in the meridional direction [Perkan et al., 2025]. The padded field is then passed through a two-dimensional (2D) convolutional layer with a  $7 \times 7$  kernel and 50 output channels, followed by a leaky rectified linear unit (Leaky ReLU) activation and 2D batch normalization. The stride is set to 1 in all convolutional layers, except in the second subblock of the first block, where it is set to 2. Before entering each subsequent subblock, the output is concatenated with the original input to the first subblock. After each block, the spatial dimensions are reduced using  $2 \times 2$  max pooling.

The encoder's output has the shape  $50 \times 11 \times 22$ , defining the latent state. Its flattened form is referred to as the latent vector  $\mathbf{z}$ , consisting of 12100 elements. This vector is modified during the data assimilation procedure (Sec. 2.3). The latent state is then passed into the decoder  $D$ , which consists of three convolutional blocks that mirror the encoder's structure, except that the final subblock in each block includes a transposed 2D convolutional layer that doubles the spatial dimensions in both latitude and longitude. The output of the final decoder block is passed through a pointwise ( $1 \times 1$ ) convolutional layer, yielding a reconstructed atmospheric field of shape  $20 \times 180 \times 360$ . A qualitative comparison between an ERA5 reanalysis field and its corresponding autoencoded version is shown in Fig. C1.

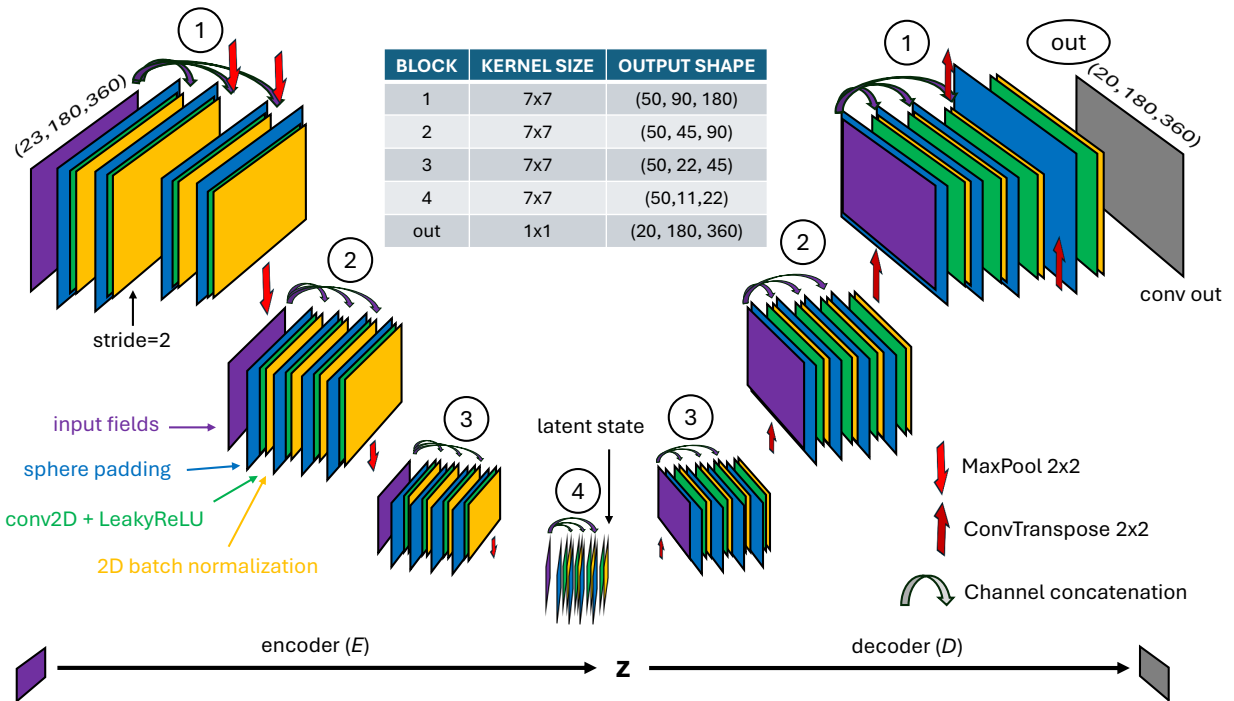


Figure A1: Autoencoder structure. The kernel sizes in the table correspond to the convolutional blocks in the downscaling/upscaling part of the network (left/right part of the scheme).

### A.2 Forecasting model

The forecasting model is a U-Net [Ronneberger et al., 2015], whose architecture is shown in Fig. A2. The network blocks have a similar design as in the AE, but the convolutional layers contain 250 channels. In the innermost layers in the downscaling part of the network,  $3 \times 3$  kernels are used instead of the larger  $7 \times 7$  ones. Additionally, blocks at the same resolution level are linked via skip connections, enabling the preservation and reuse of fine-scale features throughout the network. The NN was trained to produce 12-hour forecasts, while longer lead times were obtained by iteratively applying the model. A 24-hour forecast and its ERA5 reanalysis counterpart are compared in Fig. C2.

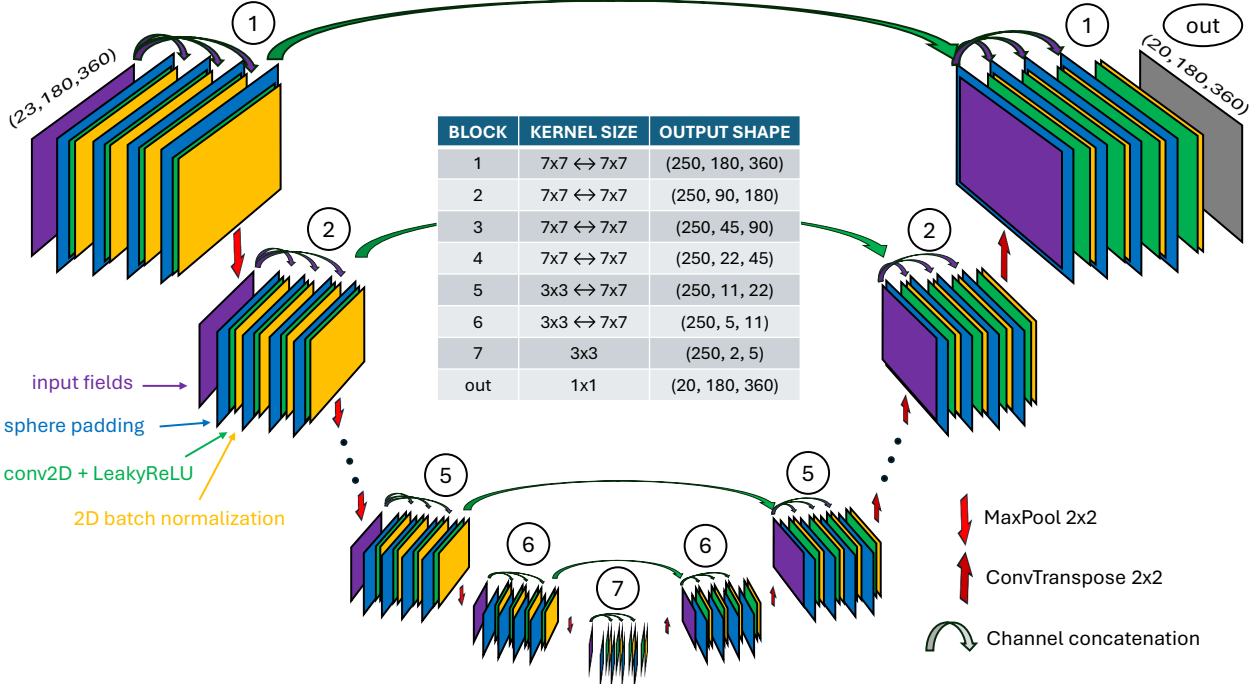


Figure A2: The structure of the neural-network forecasting model. The kernel sizes in the table correspond to the convolutional blocks in the encoding/decoding part of the network (left/right part of the scheme).

## B Appendix B: 3D-Var cost function minimization algorithm

The first guess for  $\chi$  in the minimization was a zero-vector, which corresponds to  $\mathbf{z} = \mathbf{z}_b$ . The gradient of the cost function was computed using automatic differentiation in Pytorch. The cost function was minimized using the stochastic gradient descent (SGD) optimizer with an initial step size of 0.3. The step size was halved, if  $\mathcal{J}_\chi$  increased between iterations with a lower limit of  $10^{-4}$ . Minimization terminated once the gradient norm dropped below 1 % of its initial value, typically achieved in 6 to 12 steps. The maximum number of steps allowed was 50.

## C Appendix C: Supplementary material

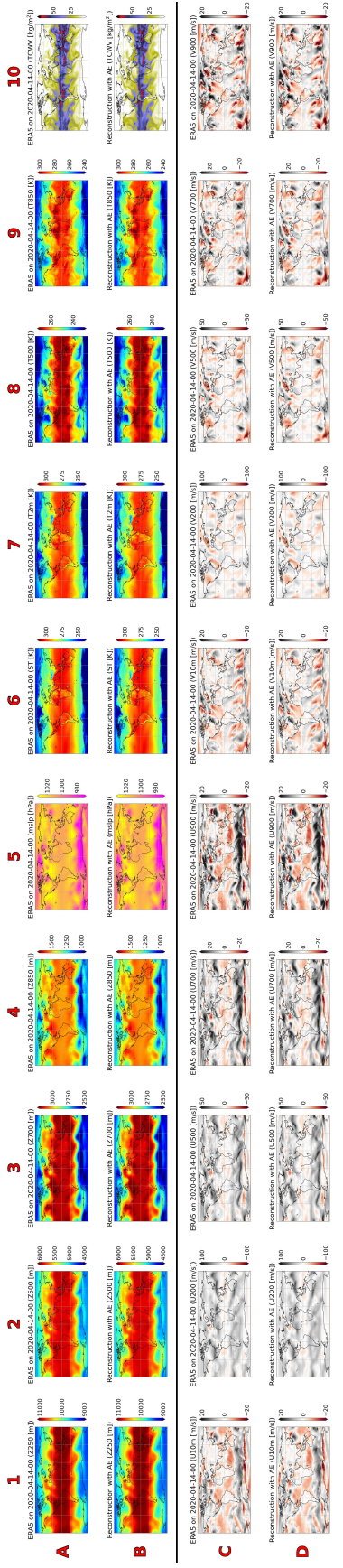


Figure C1: Comparison of the AE outputs with their targets. (A and C): ERA5 reanalysis for the 14th of April, 2020, at 00 UTC. (B and D): Autoencoded (A and C).

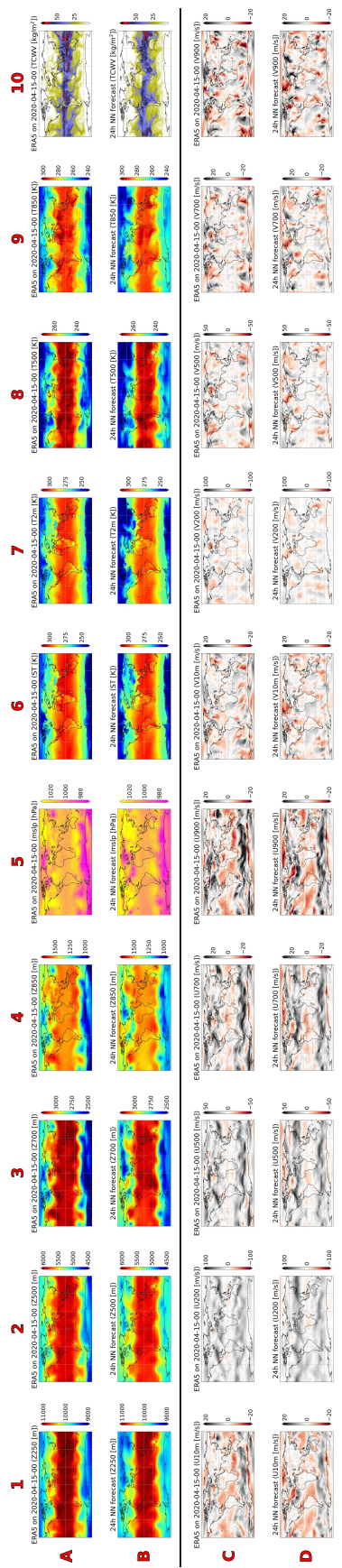


Figure C2: Comparison of the NN forecasts with their targets. (A and C) ERA5 reanalysis for the 15th of April, 2020, at 00 UTC. (B and D) 24-hour forecast, produced by the NN forecasting model, valid at the same time as (A and C).

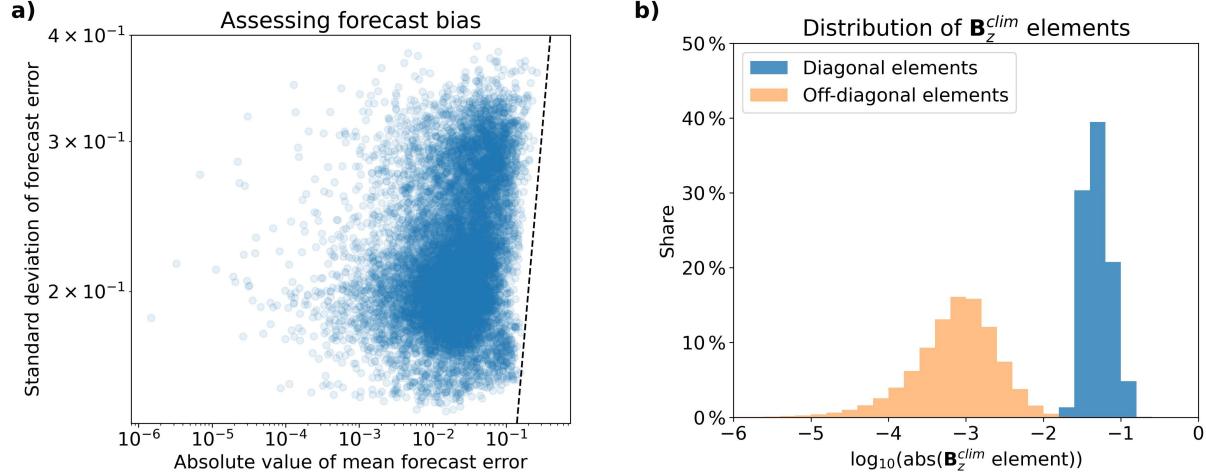


Figure C3: (a) Comparison of the forecast bias and forecast-error standard deviation for the 24-hour forecast used as the background. The horizontal axis shows the absolute mean error, and the vertical axis shows the standard deviation of the error for each of the 12100 latent vector elements. The statistics were computed over the entire validation set. (b) Distribution of  $\mathbf{B}_z^{clim}$  elements, shown with a logarithmic bin width of 0.2.

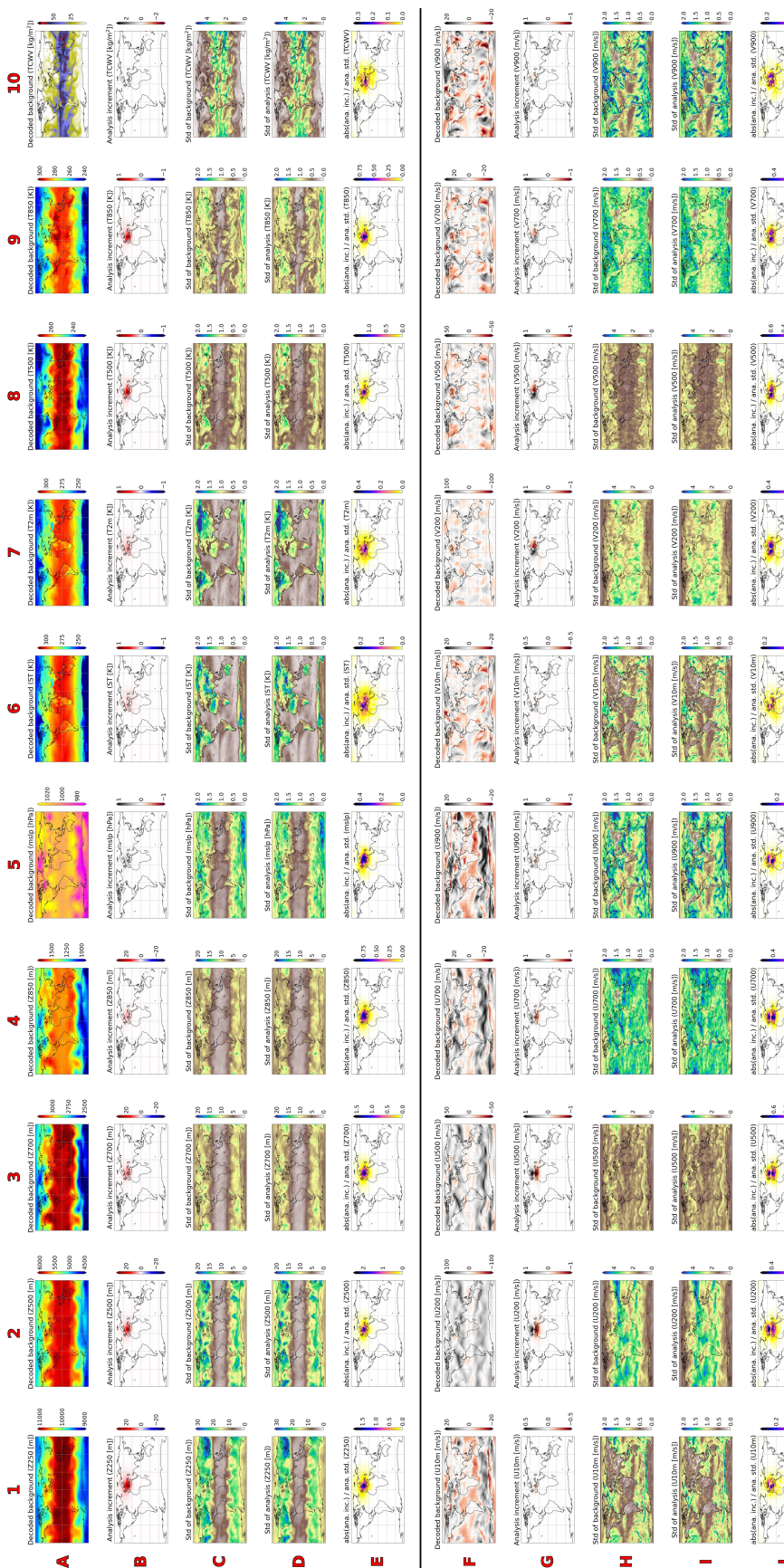


Figure C4: Single observation experiment with observed Z500 above Ljubljana with 30 m departure and 10 m standard deviation. (A and F) Decoded background for all 20 forecasted variables. (B and G) Analysis increments. (C and H) Standard deviation of background. (D and I) Standard deviation of the analysis. (E and J) Ratio between the absolute value of the analysis increment and the analysis standard deviation. To better visualize the effect on those variables that are only lightly affected by the observation (compared to the observed variable), this ratio is, in contrast to the figures in the main text, not normalized.

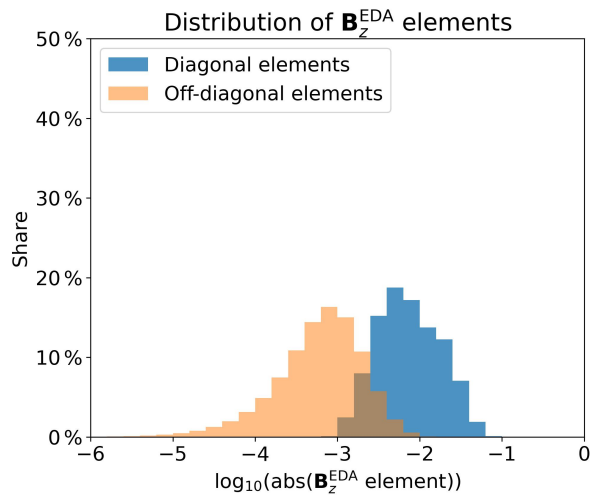


Figure C5: The distribution of  $\mathbf{B}_z^{\text{EDA}}$  elements. The bin width is 0.2 on the logarithmic scale.

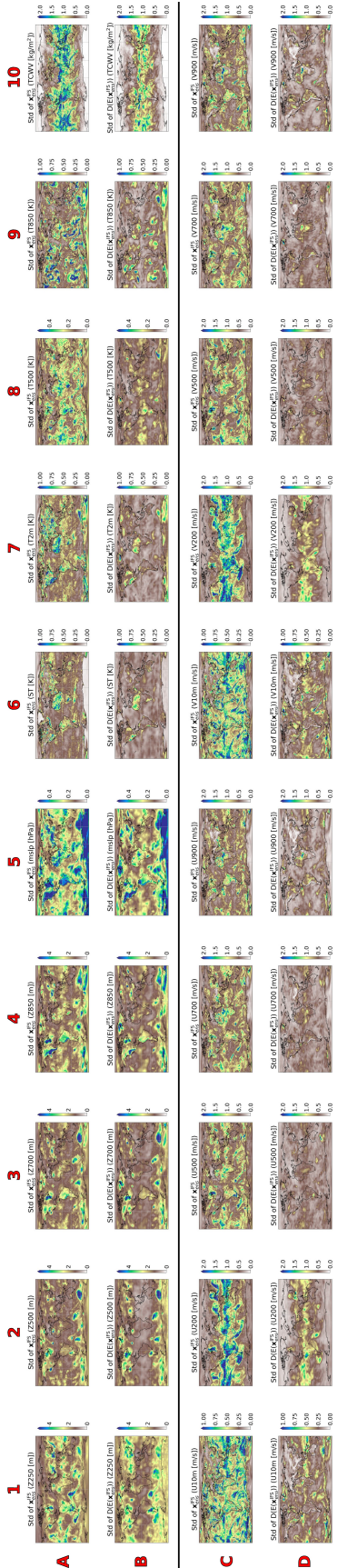


Figure C6: Standard deviation of all variables for the IFS ensemble before (A and C) and after (B and D) propagating it through the autoencoder.

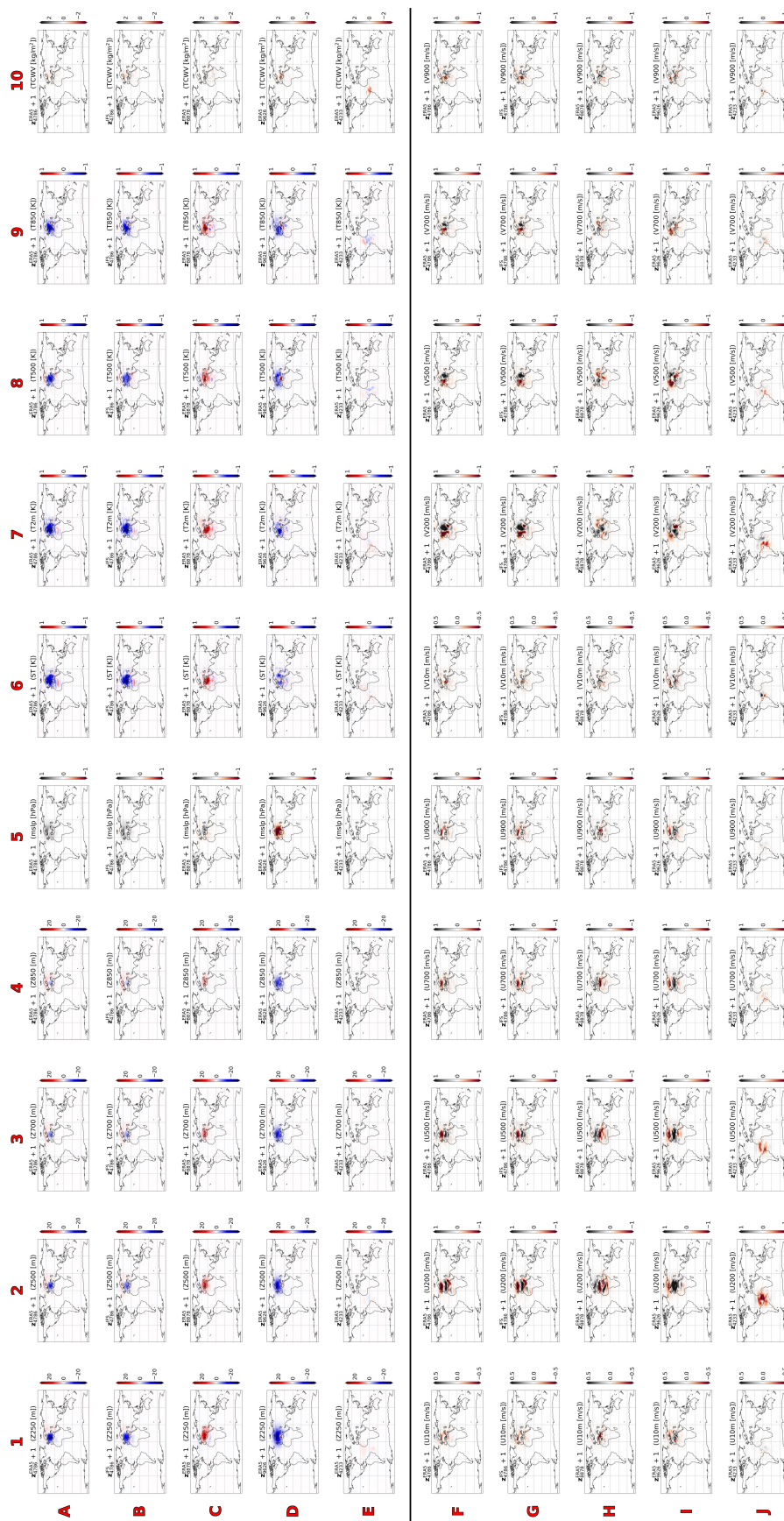


Figure C7: Changes of the decoded fields after modifying a single latent vector element. (A and F) Changes after adding 1 to the latent vector element with index 4236 of the encoded ERA5 reanalysis for the 15th of April, 2020. (B and G) As (A and F), but for the encoded first IFS ensemble member for the 14th of April, 2024. (C and H) As (A and F), but for the latent vector element with index 8878. (D and I) As (A and F), but for the latent vector element with index 9626. (E and J) As (A and F), but for the latent vector element with index 4233. The examined elements are those that are highlighted in Fig. 9.